Fall 2018

Ku-Band AG Channel Modeling

Albert Smith

KU-BAND AG CHANNEL MODELING

by

Albert Smith

Bachelor of Science
University of South Carolina, 2016

Submitted in Partial Fulfillment of the Requirements

For the Degree of Master of Science in

Electrical Engineering

College of Engineering and Computing

University of South Carolina

2018

Accepted by:

David Matolak, Director of Thesis

Mohammod Ali, Reader

Cheryl L. Addy, Vice Provost and Dean of the Graduate School

Dedication

To my parents and past teachers, the support they provided is what led me to the path I am on

Acknowledgements

I would like to recognize and thank Dr. Matolak for all the support he has provided in and out of the classroom. I can attribute my interest to wireless communication to him, and I am very thankful for having him as my undergraduate and graduate advisor. His help throughout my time as a student has been immeasurable. I would also like to thank the professors at USC during my time as a graduate student: Dr. Ali, Dr. Wong, Dr. Huray, Dr. Benigni, and (again) Dr. Matolak. Finally, I would like to recognize and thank the UAS team at NASA Glenn Research Center for allowing me to be a part of the project before and during my thesis.

Abstract

With the rise in use of Unmanned Aerial Systems (UAS), there is a need for safe and reliable integration into existing infrastructure. A proposed system for beyond line of sight control links for UAS is a Ku-band air-to-satellite communication system. To ensure this proposed system does not interfere with existing terrestrial infrastructure that operates in the Ku band, an examination of the Ku-band air-to-ground channel is required. The focus of this thesis is the modeling of the Ku-band AG channel. Tests consisting of transmitting a single tone continuous wave signal were conducted with a signal generator onboard NASA's Viking S-3 aircraft. Transmission was via a custom Ku-band monopole antenna mounted on the bottom of the aircraft's fuselage. A ground site mimicking existing terrestrial point-to-point infrastructure was used to collect received power measurements. Also included at the ground site were two wider-beamwidth antennas, to enable some assessment of multipath and polarization effects. Measurements were conducted using three inclination (elevation) angles, 0°, 2.5°, and 5°, and the aircraft was flown at three approximately constant-altitudes. The channel characteristic that was measured was attenuation, also termed path loss. Path loss estimates were made using free-space and two-ray models, and these models were refined by the inclusion of atmospheric refraction, attenuation due to fog, and curved earth models for the various flight geometries. These models were further refined by assessing angular offsets to the antenna gain patterns, as the aircraft transmitter gain patterns had deep nulls that affected measured power as the aircraft pitch varied both up and down during test flights. Measured data was then also fit

to a log-distance model for each flight test. These log-distance models are commonly used for terrestrial settings and provide a measure of goodness of fit. Overall, path loss exponents are close to the value of 2, as expected; this is the value for a free-space channel. Log-distance models yielded standard deviations in the range of 1.68 to 5.13 dB. When the inclination angle of the receiver was 5°, the measured fit equation for co-polarized antennas was found to have a path loss exponent very close to that of free-space, but as inclination angles decreased (closer to the horizon boresight), path loss exponents increased.

Table of Contents

List of Tables

List of Figures

Chapter 1. Introduction and Motivation for Measurements

1.1 Motivation

The Ku-band earth-to-space channel has been characterized and used for services such as broadcast television (DirectTV). Because Ku-band frequency systems are primarily used in ground-to-satellite links, little has been done to characterize the Ku-band air-to-ground link. A proposed method for beyond-line-of-sight control communications for unmanned aerial systems is to use an air-to-satellite Ku-band system. To ensure that this system does not interfere with existing point-to-point terrestrial infrastructure, this air-to-ground link needs to be examined. An example situation illustrating this is shown in Figure 1.1. With the channel path loss modeled, one could determine estimated received power given a link distance, antenna characteristics, and transmit power. The estimated received power at a ground site from an interfering air system could be compared to the receiver system sensitivity levels to determine if interference would occur.

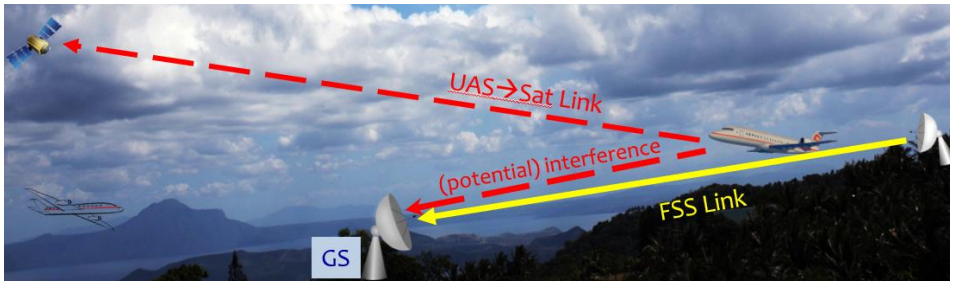

Figure 1.1 Example (potential) interference to point-to-point terrestrial link from air-to-satellite Unmanned Aerial System (UAS) [1]

1.2 Literature Review

Authors of [2] and [3] evaluate the feasibility of future Ku-band mobile systems. The authors of [2] focus on characterizing the channel as a three-state model made up of line-of-sight, shadowed, and blocked states. The shadowed state is used when foliage (primarily a single tree on the side of the road) obstructs the link, and the blocked state is used when the satellite is blocked by buildings and bridges. Measurements were made for highway, rural, suburban, and urban environments from a vehicle, and the authors found that there is a relatively high probability of being in the line-of-sight state (90% for highway and 60% for urban). They also found that leaves on a shadowing tree could cause an additional 10 dB of attenuation compared to the approximately 10 dB attenuation from a ”bald” tree, and they determined that for highway and urban environments, limited improvements could be gained from increasing the link margin (though not always practical for mobile terminals). The authors of [3] focused efforts on enhancing an existing 2-state MIMO satellite to earth model, and as a result they updated the model used in ITU-R P.681.

These works differ from the work in this thesis primarily from the use of the satellite as the transmitter. Because the transmitter is so far away (and the receiver often moving), there may be time spent outside of the ideal line-of-sight propagation, whereas the measurements made for this Ku-band study have been with a stationary receiver and a mostly line-of-sight propagation condition to an aircraft.

Authors of [4] describe measurements made for L- and C-band air-to-ground (AG) channels, and derive models from an extensive set of data. Through the use of a channel sounder (transmitter and receiver dedicated to channel measurement), this study was also

able to create wideband channel models in addition to the narrowband models. Narrowband characterization is attainable from a single tone or frequency, whereas wideband characterization requires channel information over a large bandwidth (in [3] up to 50 MHz), with the ultimate goal of wideband channels being a model for the channel's impulse response or transfer function. The work in [4] gives motivation and results for similar narrowband characterization of the AG channel, but in a different frequency band; since channel characteristics do vary as functions of frequency [5], one cannot assume identical responses in different frequency bands.

Several ITU recommendations for radio propagation were also consulted: recommendations of [6], [7], and [8] provide more information about point-to-point terrestrial links, atmospheric attenuation from fog, and atmospheric refraction. A specific ITU report [9] was also used in the analysis of the two-ray model in this thesis.

1.3 Contents of Thesis

The contents of this thesis are organized in the following manner. Chapter 2 contains a description of the measurement campaign, including test location, antennas and equipment, and transmitter and receiver configurations. Chapter 3 examines the test results in terms of measured received power. Chapter 4 contains the path loss models from the test results, and this includes actual measured path loss and several theoretical models. These models are compared and evaluated. The final chapter contains conclusions and future work.

Chapter 2. Measurement Description

The test signal was a single tone (continuous wave (CW) sinusoid) at 14.25 GHz, which is the center of the 14.0 to 14.47 GHz band allocated for the satellite communication system. Collected data was received power samples along with GPS-based location information of the aircraft. Three spectrum analyzers recorded power measurements at an approximately 8 Hz rate, and the GPS system recorded latitude, longitude, and altitude of the aircraft at a rate of 1 Hz. Figure 2.1 shows the placement of the logging computers and the layout of the equipment. Note that three receive antennas with different characteristics were used.

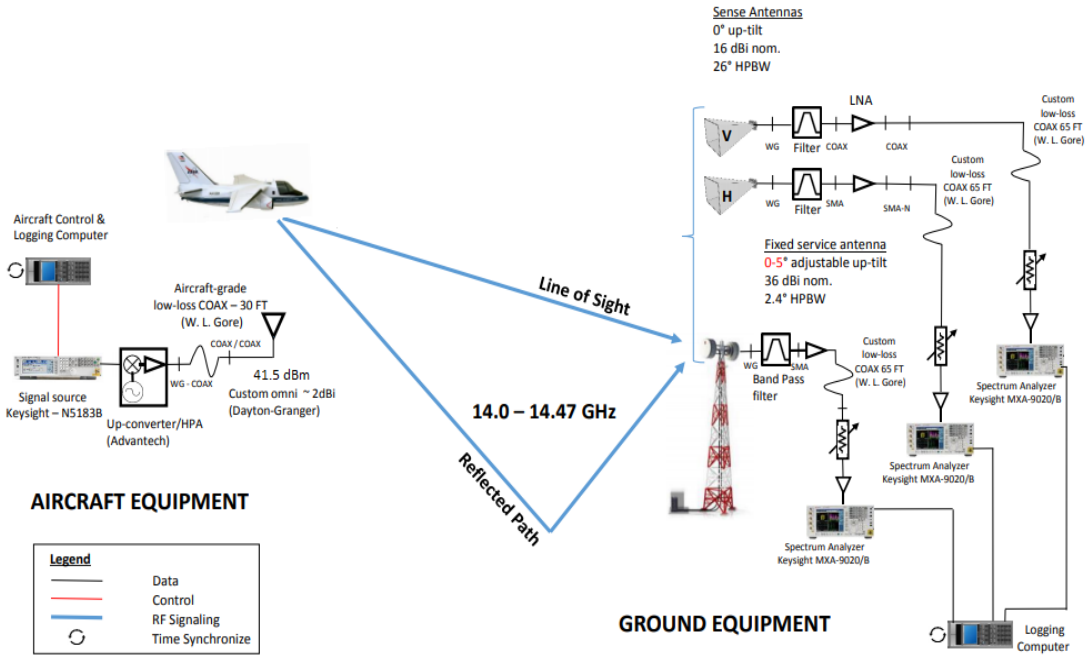

Figure 2.1 Ku-band propagation test equipment layout [10].

For accuracy in determining spatial orientations, the pointing directions of the antennas had to be calibrated. Hence, prior to recording actual flight data, the radiation boresight of the fixed service (FS) parabolic antenna—which mimics the terrestrial FS point-to-point link antennas—was pointed toward an estimated target location. This target location was 100 nautical miles from the ground station (see Figure 2.2), roughly in a south-southwest direction. The precise antenna pointing was accomplished using a precision, corrected magnetic compass to aim the antenna along a calculated true heading of 203° from magnetic north. This aiming method was known to be too crude for the very narrow beam of the FS parabolic antenna, so an additional "alignment" technique was devised to more precisely adjust the FS antenna pointing.

To align the antenna, the aircraft was flown transverse to the beam boresight and the RF signal strength at the ground receiver was recorded. As the aircraft traveled through the beam, the RF signal power rapidly maximized, and by matching this peak with aircraft position, the actual antenna boresight angle could be accurately computed. Once the pointing angle was known, the antenna azimuth could be adjusted or a new target waypoint could be calculated and relayed to the pilots. With this method, the inbound/outbound flight tracks were made parallel to the boresight of the narrow-beam GS antenna. The transverse alignment flight path segments and inbound/outbound flight tracks are visible in the flight path image of Figure 2.2.

2.1 Test Location, Rationale for Flight Paths

Flight tests were carried out in an airspace used in previous similar flight tests. This area was used during L- and C-band flight tests for the Unmanned Aerial Systems in the National Airspace System (UAS in the NAS) project for several reasons. These included

proximity to NASA GRC, availability of ground site access on NASA property, and a general lack of manmade obstructions. The local terrain is roughly categorized as both flat and hilly. This lack of structures and minimal bodies of water helps limit the amount of strong reflections. The tests were conducted on inbound (toward the GS) and outbound (away from the GS) flights directed in line with the receiver ground station at three aircraft altitudes, approximately 914.4 m, 3048 m, and 4267.2 m (3000 ft, 10,000 ft, and 14,000 ft, respectively).

Figure 2.2. Flight test location [10].

2.2 Antenna Characteristics

2.2.1 Aircraft Antenna (Dayton-Grainger)

Mounted on the bottom of the aircraft is a vertically-polarized, quarterwave, omnidirectional antenna, shown in Figure 2.3. Coordinate axes are defined as follows: the x-axis for the antenna points forward toward the cockpit, the y-axis points towards the right wing, and the z-axis points downward away from the aircraft. The manufacturer (Dayton-Grainger) reported a gain of >3 dBi via simulations conducted in High-Frequency Structure Simulator (HFSS) software. Prior to mounting the antenna on the aircraft, the antenna's performance was measured at the NASA GRC Far-Field Antenna Test Range to complete a 3D pattern. The chamber set up is shown in Figure 2.4. For zero x-y plane rotation (a zero degree "phi-cut"), a maximum gain of 5.2 dBi was measured at -61 degrees, seen in Figures 2.5 and 2.6.

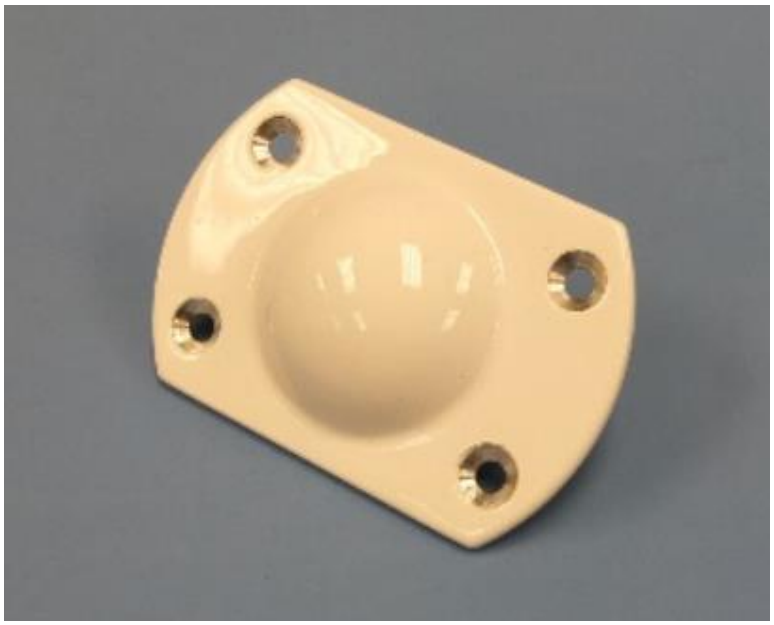

Figure 2.3. Dayton-Grainger Aircraft-Grade Monopole Ku-band Antenna [10].

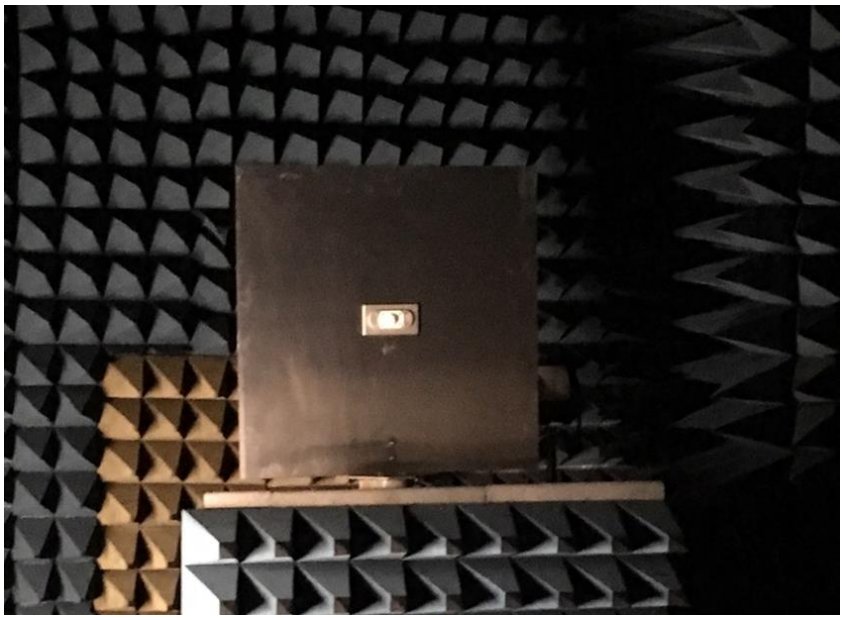

Figure 2.4. Antenna in anechoic chamber, with mounting on ground plane, simulating fuselage of aircraft [10].

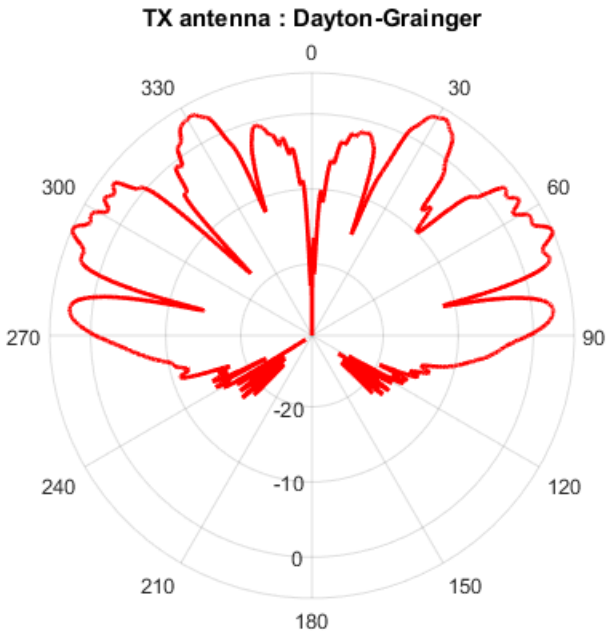

Figure 2.5. Transmitter antenna gain polar plot in dBi for a zero x-y rotation (plane containing cross-section used during inbound and outbound flight test). Here 0 degrees would be pointing down and away from the aircraft fuselage.

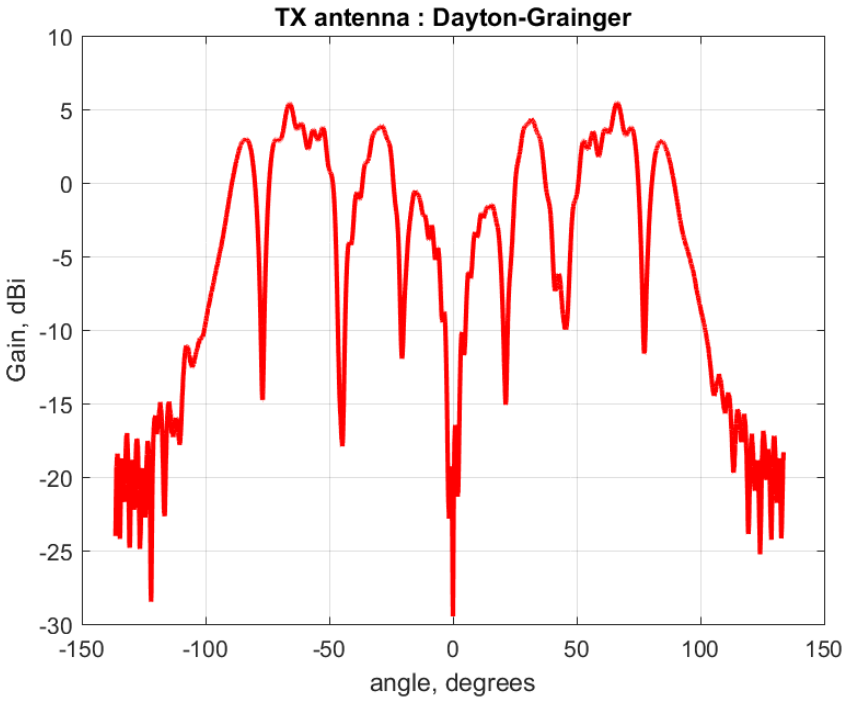

Figure 2.6. Transmitter antenna gain vs. elevation angle for a zero x-y rotation (plane containing cross-section used during inbound and outbound flight test).

2.2.2 Fixed Service Satellite Parabolic Antenna (Commscope)

The ground site receiver antenna similar to the Fixed-Service antennas (of the existing point-to-point Ku-band terrestrial infrastructure), was a 2-ft (0.6096 m), vertically-polarized, parabolic reflector (Commscope model VHLP2-15-3WH/B), shown in Figure 2.7. The manufacturer specifies the half power beamwidth to be 2.5 degrees. This antenna was also tested at NASA GRC, and far-field pattern data was collected for +/- 60 degrees in elevation and azimuth angle, relative to boresight. The beamwidth follows the manufacturer specifications, and a maximum gain of 37.5 dBi was measured. Antenna patterns are shown in Figure 2.8 (polar coordinate system) and 2.9 (cartesian coordinate system), and both coordinate systems are included to emphasize the narrowness of the beamwidth and facilitate the reading of values.

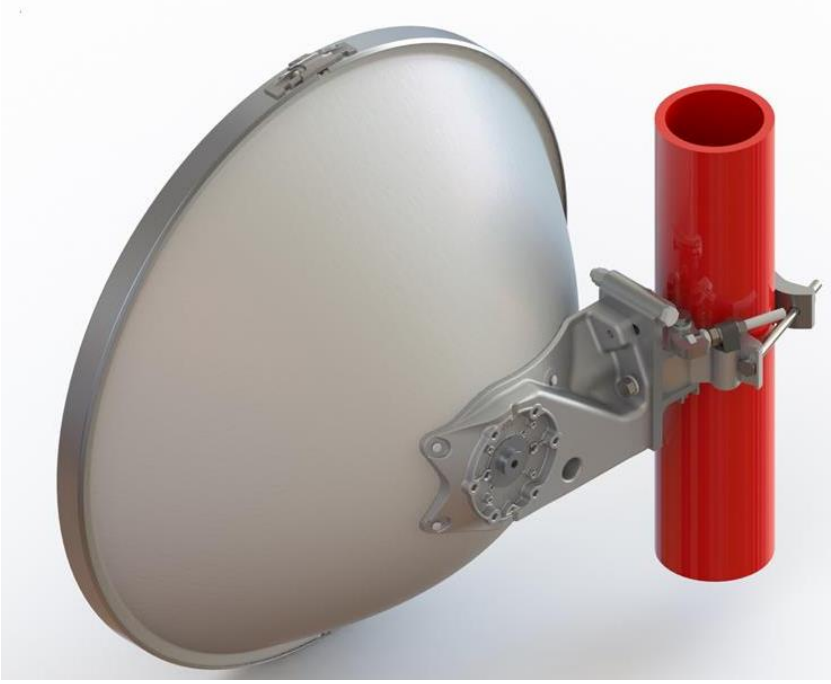

Figure 2.7. Commscope model VHLP2-15-3WH/B “Fixed Site” (FS) ground station Ku band antenna [11].

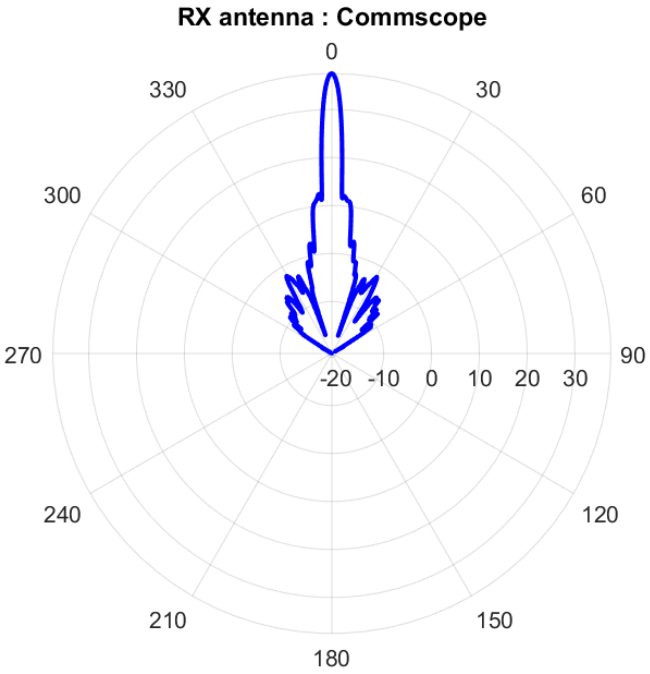

Figure 2.8. Receiver antenna gain polar plot in dBi for elevation plane (plane containing cross-section used during inbound and outbound flight test). Here 0 degrees points in the direction of the antenna boresight.

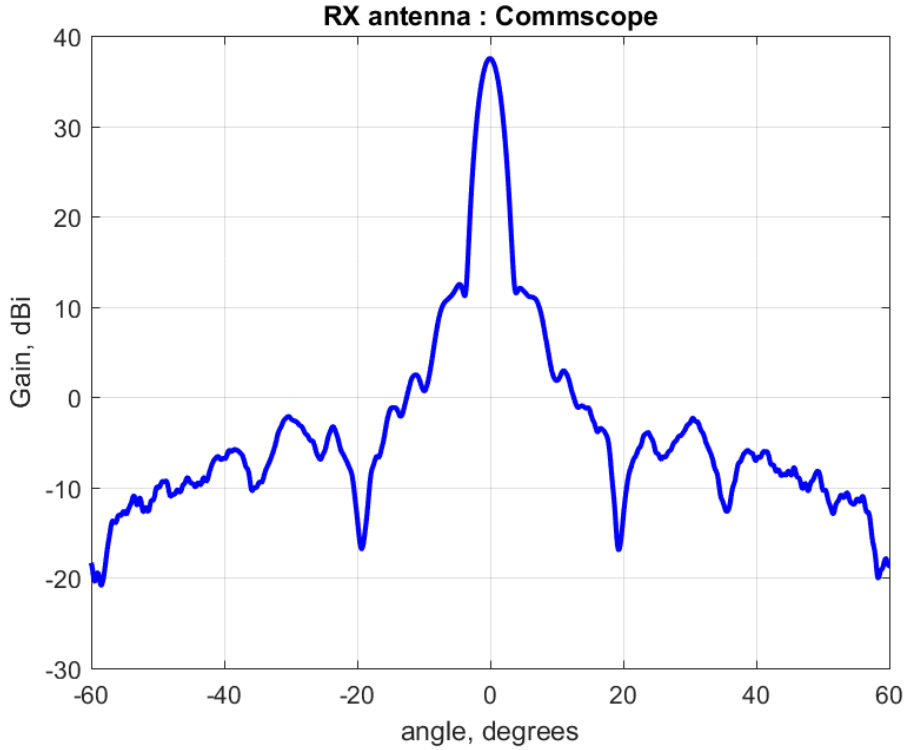

Figure 2.9. Receiver antenna gain rectangular plot for elevation plane.

2.2.3 Vertical and Horizontal Horn Antennas (ARA)

Two horn antennas (ARA model MWH-1218/A) were also used during the test. These antennas were mounted on either side of the parabolic reflector, and were used to enable capture and examination of multipath reflections in more detail; they were chosen due to their larger half power beamwidth (26.5 degrees for the elevation plane and 26.8 degrees for the azimuth plane). Figures 2.10 and 2.11 show the horn antenna elevation and azimuth patterns, respectively.

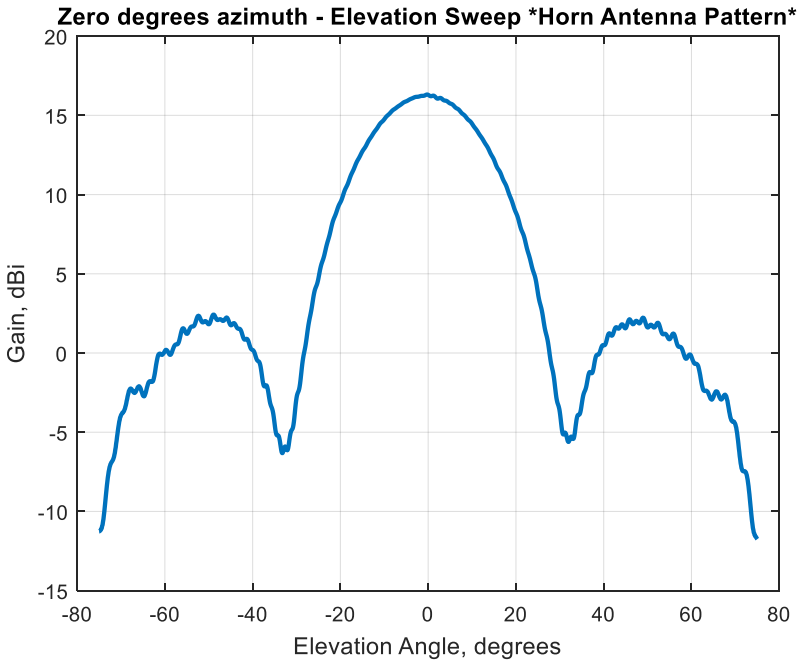

Figure 2.10. ARA Horn antenna gain plot for the elevation plane (plane used in inbound and outbound flight tests for vertically polarized horn antenna).

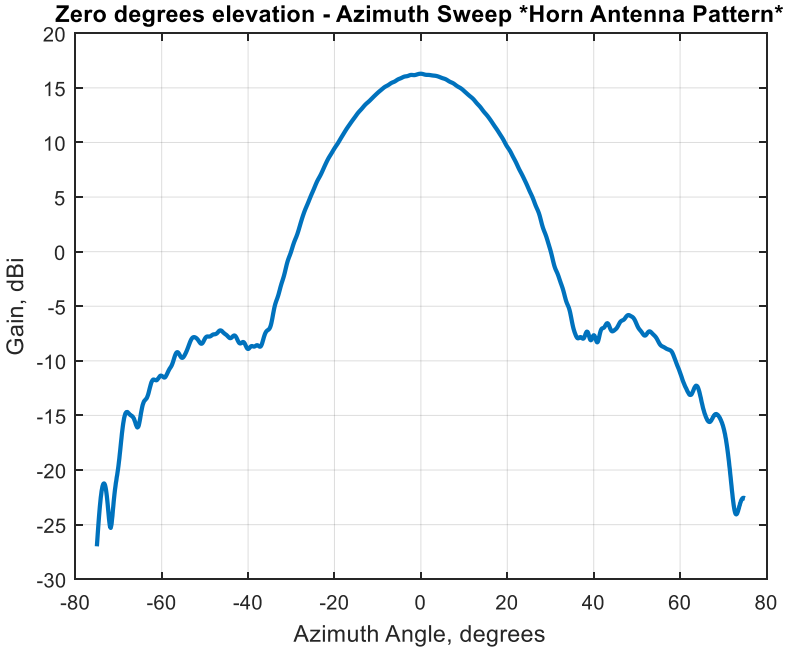

Figure 2.11. ARA Horn antenna gain plot for the azimuth plane (plane used in inbound and outbound flight tests for horizontally polarized horn antenna).

2.3 Transmitters and Receivers

2.3.1 Transmitter

The transmitter consisted of a Keysight N5183B signal generator transmitting an unmodulated continuous-wave signal at 14.25 GHz. This was fed into an Advantech up-converter and high power radio frequency (RF) amplifier. The high power amplifier was connected to the transmitting antenna with an aircraft-grade low-loss 30 foot coaxial cable produced by Gore. The transmitting aircraft antenna was the custom omnidirectional antenna from Dayton-Grainger with approximately a 5 dBi gain. The power level at the antenna feed was 41.5 dBm. The transmitter chain equipment was carried on NASA's S-3B Viking aircraft; see Figure 2.12.

Figure 2.12. Antenna mounting location for the Viking S-3B [10].

2.3.2. Receiver

As noted, the receiving ground station consisted of three antennas. The primary antenna for the test was the parabolic reflector antenna (Commscope Model VHLP2-15-3WH/B). From the Commscope antenna, the feed structure was as follows: a waveguide connected to a bandpass filter, which connected by SMA adapter to a low noise amplifier, followed by a custom low-loss coaxial 65 ft Gore cable, which connected to the final receiver component, a signal analyzer (Keysight N9030A). The total cascaded gain of the receiver components from antenna port (shown as A in Figure 2.13) to signal analyzer (shown as B in Figure 2.13) is 37.9 dB. The power level at the antenna feed is then 37.9 dB lower than the value logged in the data files by the signal analyzer.

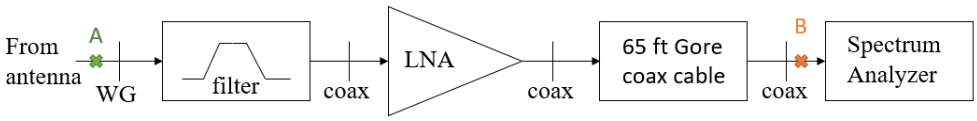

Figure 2.13. Block diagram of receiver components. WG indicates the connection was a waveguide and coax indicates the connection was by coaxial cables and connectors.

The other two receiver antennas were horn antennas (ARA MWH-1218/A). These horns were identical in make, with one rotated 90 degrees, such that one would receive predominantly vertically polarized signals and the other would receive predominantly horizontally polarized signals. All these antennas were mounted side by side, and placed on a mast that was 10 m tall, and able to incline at desired levels; these levels for the test were 0, 2.5, and 5 degree angles of elevation. Figure 2.14 shows a photograph of the antennas atop the mast. Software defined radios were configured to log data from the spectrum analyzers connected to the two horn antennas.

Figure 2.14. Receiver ground station antenna mast with Commscope parabolic antenna mounted with vertical and horizontally polarized horn antennas on either side [10].

Chapter 3. Test Results

In this chapter, the measured test results will be described, as well as governing equations used for estimating received power with free-space and 2-ray channel models. First the geometry used to determine incoming and outgoing beam angles will be described. These angles are used to determine receiver antenna gains, G_{rx}, and transmitter antenna gains, G_{tx}, which are used in the link budget in equation (3.1). Next, effects from atmospheric refraction are examined. Also described are the effects of fog attenuation. Lastly, potential angle offsets are explained and explored.

$$P_{rx} = P_{tx} + G_{rx} + G_{tx} + G_{c,amplifier} - L_c - L_{path} \tag{3.1}$$

The transmitting power, P_{tx}, was 41.5 dBm. The combined cable losses L_c and cable amplifier gains $G_{c,amplifier}$ was +37.9 dB (see Figures 2.1 and 2.13). The estimated received power, P_{rx}, can be found with theoretical path loss, L_{path}. The measured path loss was determined from measured received power. The different path loss models will be discussed in chapter 4.

3.1 Flat Earth Geometry

The reference [12] was used to determine the link distance for the earth-surface reflected path and the arrival and departure angles for the line-of-sight (LOS) and 2-ray components with the assumption that the Earth is flat. With knowledge of the antenna gain patterns, accurate gains can be determined for LOS arrival and departure angles and

reflected component arrival and departure angles. These gains were used in link budget equations to estimate received power, as well as determine the free-space and 2-ray path losses.

3.2 Curved Earth Geometry

For long link distances, the flat Earth assumption fails to hold. A later section dealing with curved Earth geometry in the reference [12] is used for determining the curved Earth link distances and arrival and departure angles for both line-of-sight and reflected components. These angles will be more accurate than those computed by the flat-earth model, due to the more accurate geometry used, and they will be used to determine antenna gains. These antenna gains were used in a link budget to estimate received power and find free-space and 2-ray path losses.

To determine reflection coefficients needed for two ray analysis the references [6] and [9] are used. Additionally to determine incoming and outgoing reflected beam angles, a figure (shown in Figure 3.1) from [9] is used. The corresponding variables in Figure 3.2 for our test conditions are as follows: h_1 is the transmitter height, h_2 is the receiver height, ϕ is the grazing angle formed by the reflected beam and tangent to the ground, line segment $\overline{\mathrm{OE}}$ is the sum of transmitter height and effective earth radius (where the effective earth radius, r, is equal to ka, with k being the Earth radius modifier and a being the mean Earth radius 6378.137 km), θ_D is the departure angle formed by the outgoing reflected beam, and θ_A is the arrival angle formed by the incoming reflected beam.

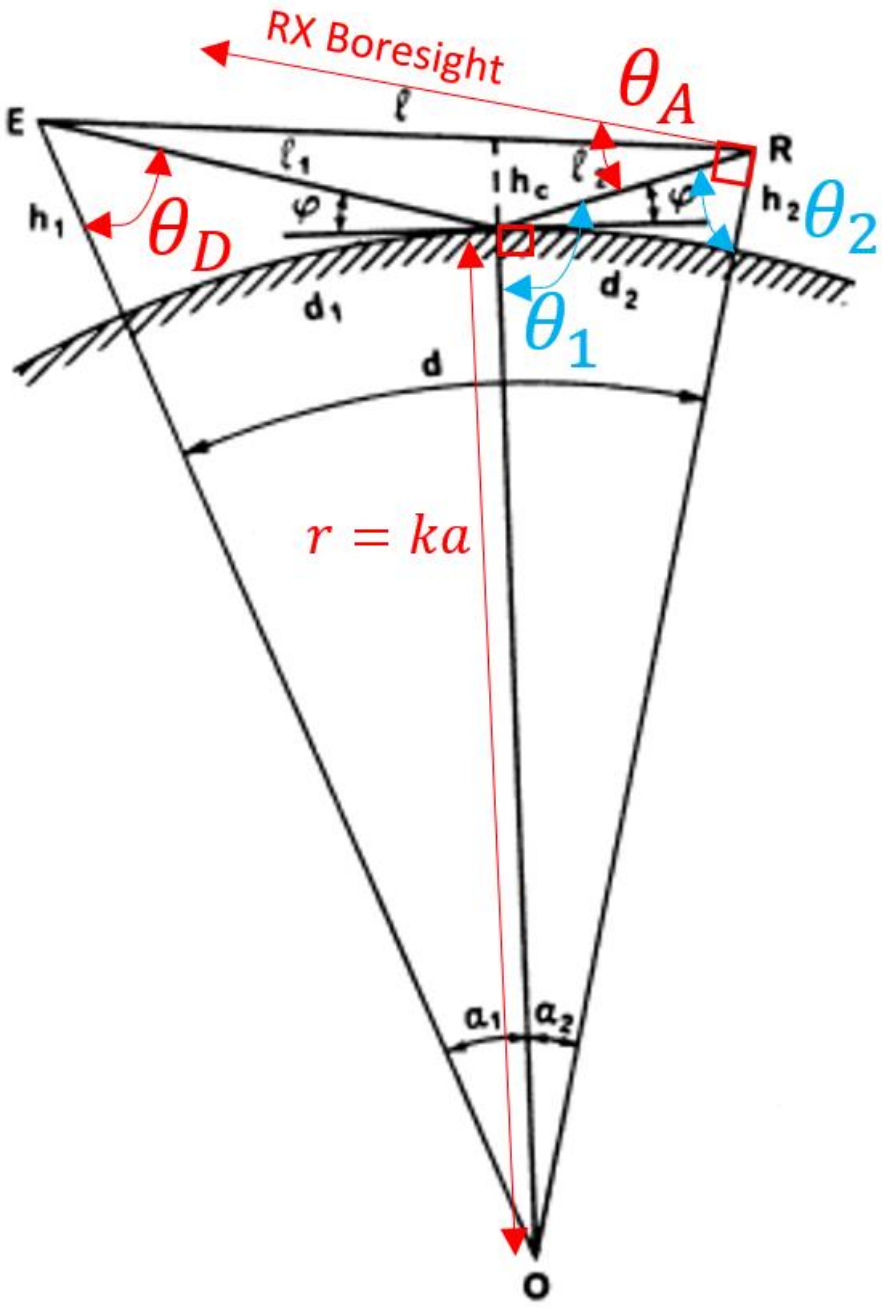

Figure 3.1. Curved earth geometry for two ray analysis
modified from [9].

An intermediate angle, θ_1 can be determined from known angles, since it is a combination of a right angle (formed by a line tangent to the ground at the reflection point

and a line at the same point directed to the center of the Earth, seen in Figure 3.1) and the grazing angle:

$$\theta_1 = 90° + \phi. \tag{3.2}$$

Then from interior angle summation of a triangle, shown in (3.3) a second intermediate angle θ_2 can be found, shown in (3.4).

$$\alpha_2 + \theta_2 + \theta_1 = 180° \tag{3.3}$$

$$\theta_2 = 180° - \theta_1 - \alpha_2 \tag{3.4}$$

The arrival angle of the reflected beam from antenna boresight (aimed at the horizon) can then be calculated as (3.5).

$$\theta_A = -(90° - \theta_2) \tag{3.5}$$

This will be the angle used to calculate the gain of the incoming reflected ray. Note that this angle is negative with respect to antenna boresight since it is below the horizon of the antenna.

An alternate procedure can be used on the transmitter side to determine the departure angle of the reflected beam, but fewer intermediate steps are required. With α_1 known, l_1 can be determined from the law of cosines, shown in (3.6):

$$l_1^2 = (r + h_{tx})^2 + r^2 - 2r(r + h_{tx})\cos(\alpha_1)\,. \tag{3.6}$$

Using the law of sines (3.7), the angle from antenna null (normal to aircraft body, aimed at ground) θ_D can be found, which is shown in (3.8).

$$\frac{r}{\sin\left(\theta_{2nd-ray-departure}\right)} = \frac{l_1}{\sin(\alpha_1)} \tag{3.7}$$

$$\theta_D = \arcsin\left(\frac{r\,sin(\alpha_1)}{l_1}\right) \tag{3.8}$$

As a check, the departure angle can also be found as described for the receiver by taking the summation of interior triangle angles, using a temporary angle made up of a right angle and the grazing angle of reflection.

Using the arrival and departure angles found for the LOS beam (found in reference [12]), arrival and departure angles for the reflected beam (shown in (3.5) and (3.8)), and the gain pattern for the antennas, the antenna gains can be accurately determined for the LOS component and the reflected component. The received power can then be estimated by the link budget shown in (3.1). For a free-space channel estimate, the LOS gains can readily be used in the link budget equation. For the two-ray channel estimate, see chapter 4, as it is slightly more complex. A comparison between received power measured data, and that estimated from flat Earth and curved Earth, is shown in Figure 3.2.

When the link distances become large, the flat earth and curved earth results diverge. One cause of the difference is due to differing calculated antenna gains. The curved Earth estimate yields differing values for arrival and departure beam angles than does the flat Earth estimate. These angles are the defining factor for the antenna gains values used in the link budget analysis. Since it is accepted that the curved earth approximation is more appropriate, especially when large distances are involved, only the curved earth estimates will be shown in subsequent plots. In general, we expect to have received power decrease with increasing link distance, but that is not the case in Figure 3.2

due to the extreme directionality of the parabolic antenna. From 20 km to 60 km, the aircraft is moving closer to the center of the main antenna lobe, which is increasing the receiver LOS gain, resulting in a higher measured power.

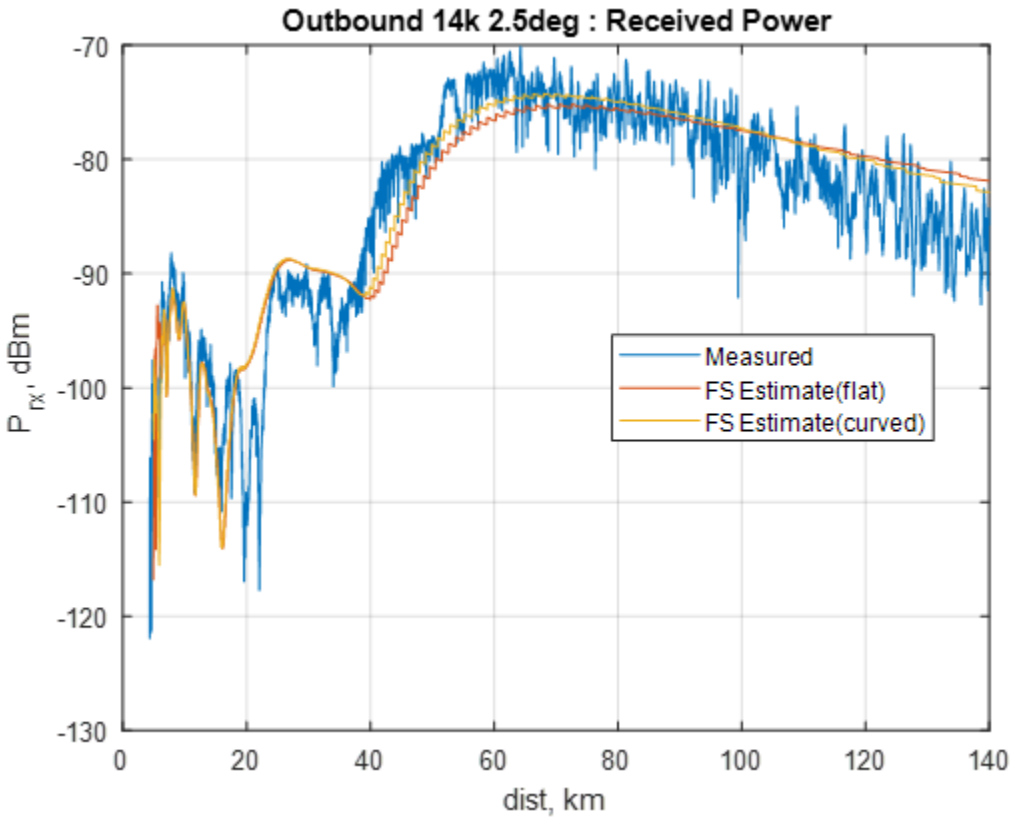

Figure 3.2. Received power versus link distance.

3.3 Atmospheric Refraction Effects

In the standard curved earth model, the earth radius is modified by k to determine the effective earth radius. This effective earth radius modifier has a typical value of 4/3. This modifier must be altered to account for atmospheric refraction. The equation (3.9) from [8] can be used to determine k when accounting for atmospheric refraction with knowledge of the refractive index, n.

$$\frac{1}{ka} = \frac{1}{a} + \frac{\mathrm{d}n}{\mathrm{d}h} \tag{3.9}$$

Inverting and solving (3.9) for k yields (3.10).

$$k = \frac{\frac{1}{a}}{\frac{1}{a} + \frac{\mathrm{d}n}{\mathrm{d}h}} = \frac{1}{1 + a\frac{\mathrm{d}n}{\mathrm{d}h}} \tag{3.10}$$

Reference [13] gives the relationship between refractive index, n, and height, h, as equation (3.11).

$$n(h) = 1 + N_0 10^{-6} \mathrm{e}^{-\frac{\mathrm{h}}{\mathrm{h}_0}}, \tag{3.11}$$

where N_0 is the average value of atmospheric refractivity at sea level, and it has a value of 315. The value of the scale height h_0 is 7.35 km. The refractive gradient can be found by taking the derivative of the refractive index, shown in (3.12).

$$\frac{\mathrm{d}n}{\mathrm{d}h} = N_0 10^{-6} e^{-\frac{h}{h_0}} \frac{-1}{h_0} = -\frac{10^6 N_0}{h_0} e^{-\frac{h}{h_0}}. \tag{3.12}$$

An average modifier k can then be found by using the midpoint of the receiver height and the average transmitter height, and this value was determined to be 1.2542 for 14,000 ft altitude. Figure 3.3 shows the difference between using the typical value of 4/3 and the altitude specific value for *k*, and Figure 3.4 shows a zoomed in view to highlight the small difference between the two estimates.

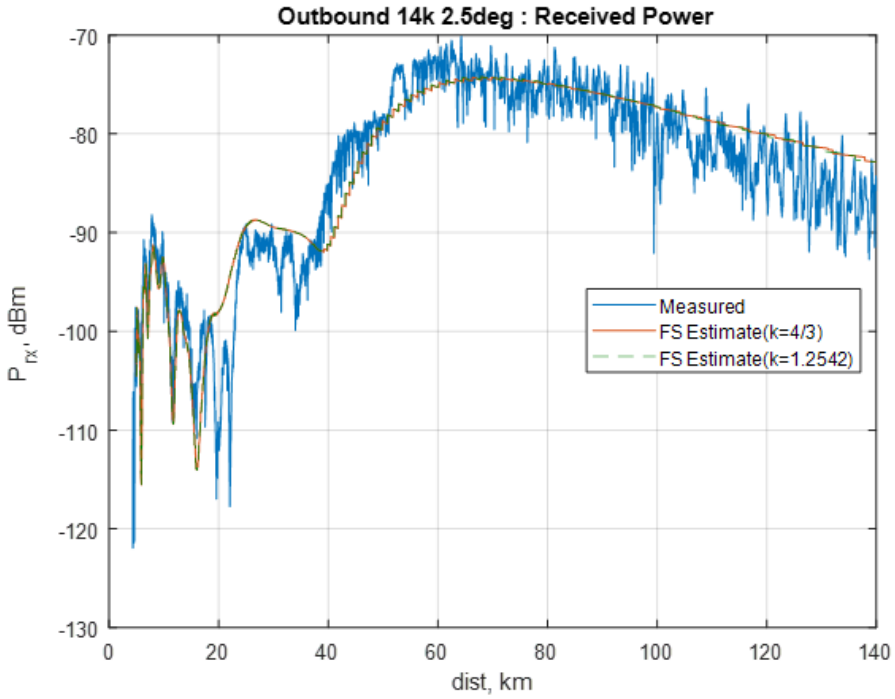

Figure 3.3 Received power versus link distance comparing standard curved earth model and atmospheric refraction curved-earth model.

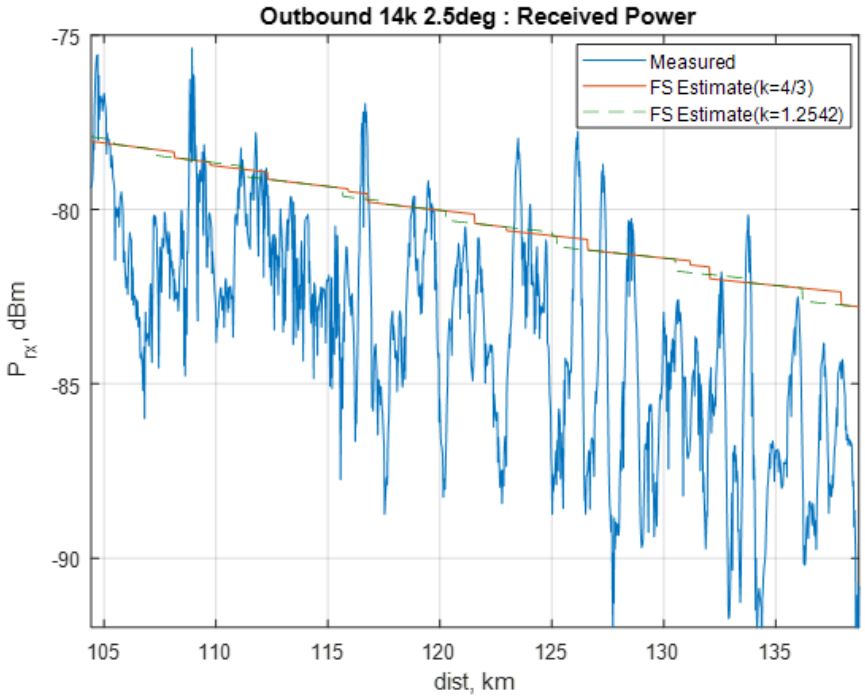

Figure 3.4. A zoomed in view of Fig. 3.8. highlighting the difference between the curves.

The difference between the curved earth model and that model with inclusion of atmospheric refraction is extremely small. There difference in the radius modifier factors for the given flight track is approximately 0.079 (relative to typical value of 4/3), though it will differ with aircraft altitude (lowest altitude flights give a difference of 0.013). While the difference is almost indistinguishable, the following plots will use the model that includes the refraction as it does not significantly impact calculation runtime.

3.4 Attenuation from Fog

The NASA engineers conducting the flight tests noted that the weather conditions were quite foggy. The document [8] provides methods for determining attenuation within clouds, and fog can be modeled as low hanging clouds. The specific attenuation (in dB/km) for fog is given as follows:

$$\gamma_{fog}(f,T) = K_l(f,T)M. \tag{3.13}$$

In this equation, K_l is the cloud liquid water specific attenuation coefficient (in dB/km/(g/m^3)) and is dependent on frequency f (in GHz) and temperature T (in K), and M is liquid water density in the fog (g/m^3). The document gives two values for M: for a medium fog (with visibility of 300 m) M=0.05 g/m^3, and for a thick fog (with visibility of 50 m) M=0.5 g/m^3. For our estimate we will use the midpoint between these values as 0.225 g/m^3. This value was found to produce good agreement with measurements. The temperature is based on the measured temperature at Cleveland-Hopkins International Airport. The ITU document [8] gives a Rayleigh scattering model to determine K_l, and this holds up to a frequency of 200 GHz,

$$K_l(f,T) = \frac{0.819f}{\epsilon''(1+\eta^2)}, \tag{3.14}$$

$$\eta = \frac{2+\epsilon'}{\epsilon''}, \tag{3.15}$$

where *f* is frequency in GHz, and the complex dielectric permittivity of water is given by a double-Debye model:

$$\epsilon''(f) = \frac{f(\epsilon_0 - \epsilon_1)}{f_p\left(1+\left(\frac{f}{f_p}\right)^2\right)} + \frac{f(\epsilon_1 - \epsilon_2)}{f_s\left(1+\left(\frac{f}{f_s}\right)^2\right)} \tag{3.16}$$

$$\epsilon'(f) = \frac{(\epsilon_0 - \epsilon_1)}{\left(1+\left(\frac{f}{f_p}\right)^2\right)} + \frac{(\epsilon_1 - \epsilon_2)}{\left(1+\left(\frac{f}{f_s}\right)^2\right)} + \epsilon_2 \tag{3.17}$$

$$\epsilon_0 = 77.66 + 103.3(\theta - 1) \tag{3.18}$$

$$\epsilon_1 = 0.0671\epsilon_0 \tag{3.19}$$

$$\epsilon_2 = 3.52 \tag{3.20}$$

$$\theta = \frac{300}{T} \tag{3.21}$$

with T the temperature in Kelvin. Two relaxation frequencies (in GHz), the principal f_p and secondary f_s are given as follows:

$$f_p = 20.20 - 146(\theta - 1) + 316(\theta - 1)^2, \tag{3.22}$$

$$f_s = 39.8 f_p. \tag{3.23}$$

Since the cloud attenuation is based on distance through the fog, the short link distance values will not be altered by a significant value, but as the link distance increases

beyond 20 km the effect is quite visible. The liquid water specific attenuation coefficient was found to be 0.0994 dB/km/(g/m^3), and the cloud attenuation constant was found to be 0.024 dB/km. Figure 3.5 gives a range of the attenuation values, with the largest value being slightly higher than 3 dB of loss at a link distance of 140 km. The inclusion of fog attenuation modifies the link budget to become,

$$P_{rx} = P_{tx} + G_{rx} + G_{tx} + G_{c,amplifier} - L_c - L_{path} - \gamma_{fog}\left(\frac{R_{los}}{1000}\right), \qquad (3.24)$$

where R_{los} is the link distance in meters. Figures 3.6 and 3.7 show how received power estimates with fog losses fit more closely with measured data. At short distances (less than 20 km), nothing changes because fog loss depends on link distance, and at large distances better agreement is shown when fog losses are included.

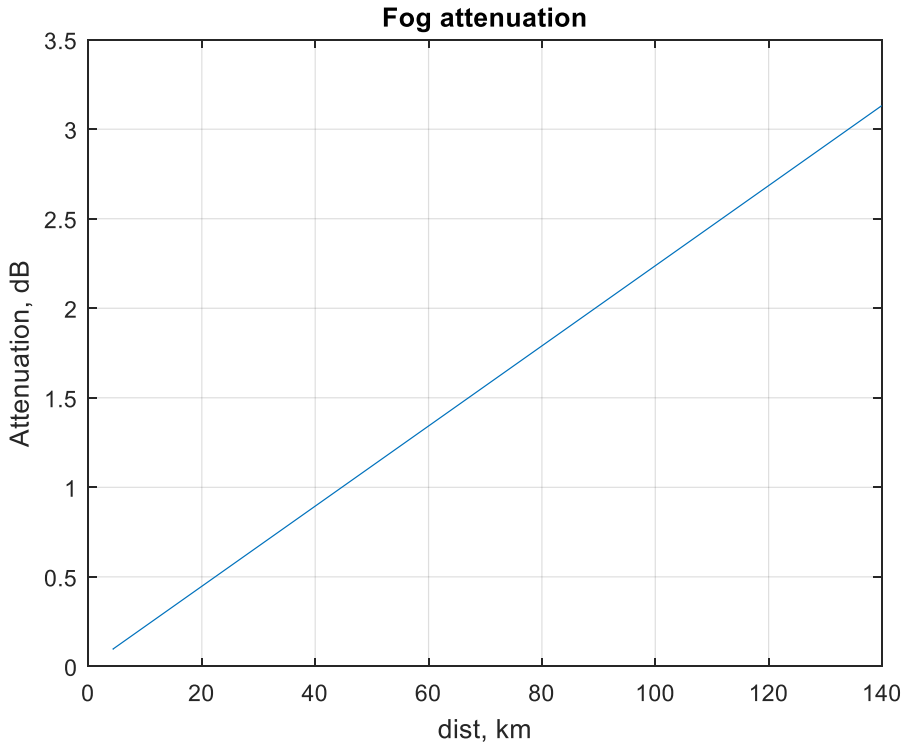

Figure. 3.5. Fog attenuation versus link distance.

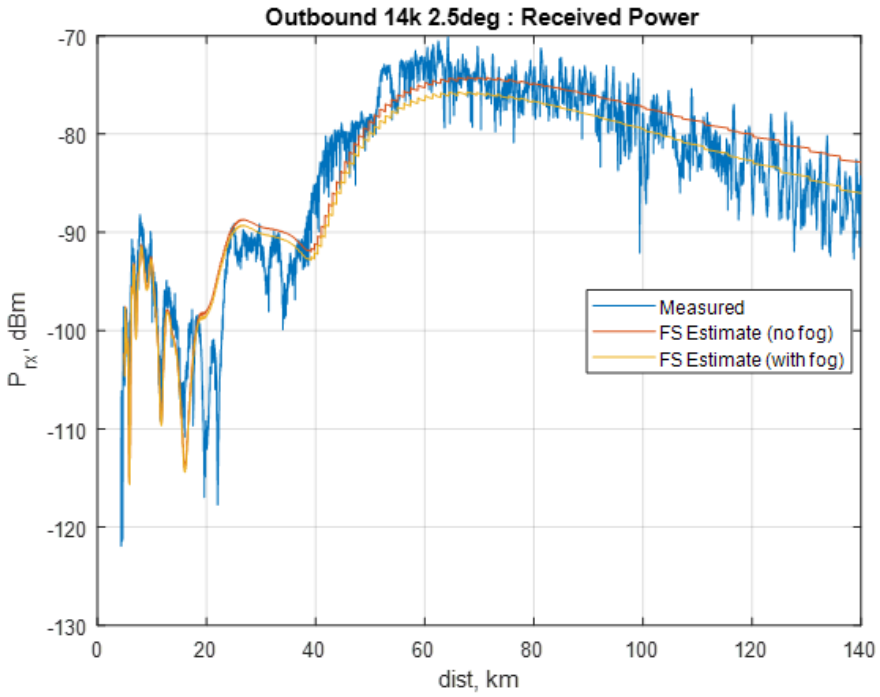

Figure 3.6. Received power versus link distance comparing with and without fog attenuation for an outbound flight.

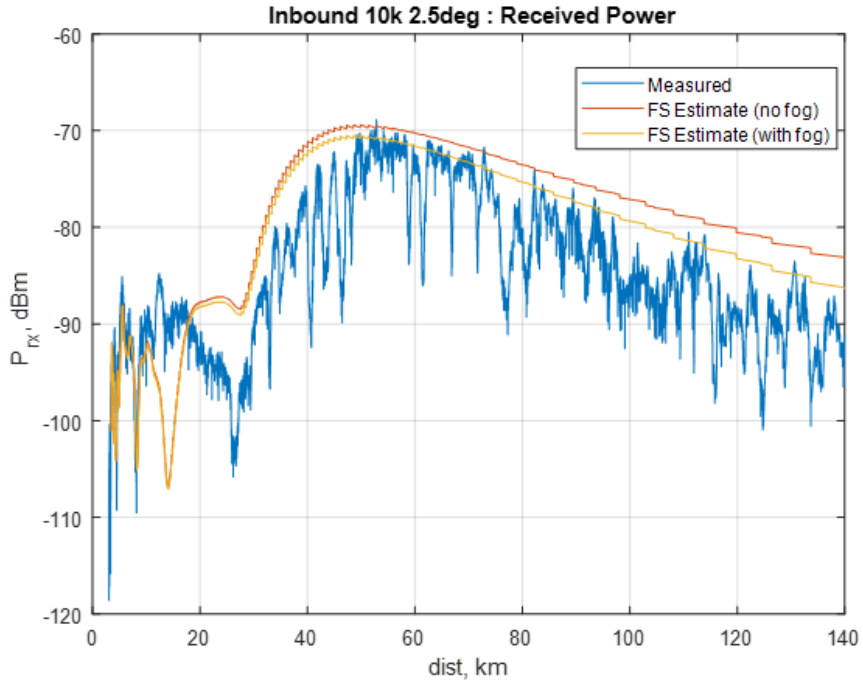

Figure 3.7. Received power versus link distance comparing with and without fog attenuation for an inbound flight.

3.5 RX and TX Antenna Angular Offsets

Despite the best efforts to align, some offsets may still be present. During the tests, the aircraft is slightly pitched up to maintain altitude at low speed, so an offset may be required on the transmitter angle (an example is shown in Figure 3.8). Similarly, an offset might be needed for the receiver antenna angle if the local ground was unlevel or inclinometer had not recently undergone calibration. In general, the receiver antenna angle offset (if included) would be the same for each set of tests, and the transmitter angle offset (if included) would vary from test to test because the aircraft might be pitched at different angles for different speeds for each altitude. In practice the transmitter antenna angle (due to the aircraft pitch) would vary continuously during the test, but the plots included use a single average value of offset applied to all points. Figures 3.9 and 3.10 show comparisons of flight tracks with and without the offsets, and they show much better agreement with the angle offsets, especially between 0 km and 40 km.

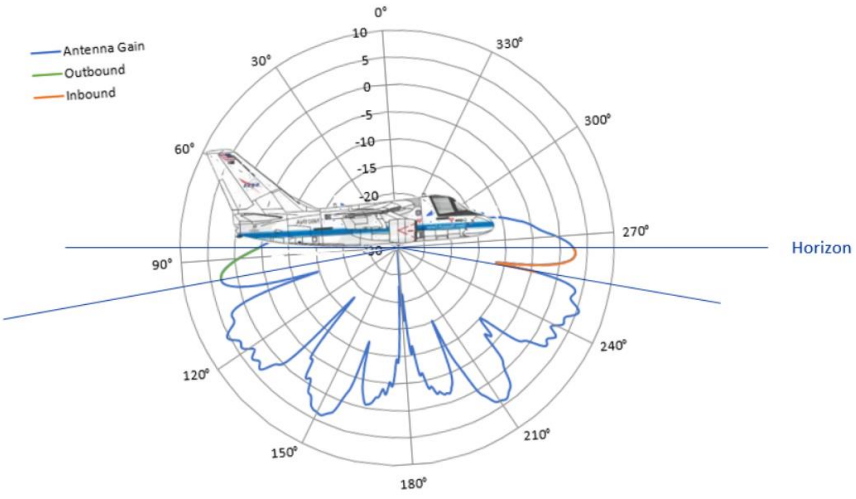

Figure 3.8. Pitched up aircraft, with the 90 and 270 degree lines of the aircraft no longer in-line with the horizon [10].

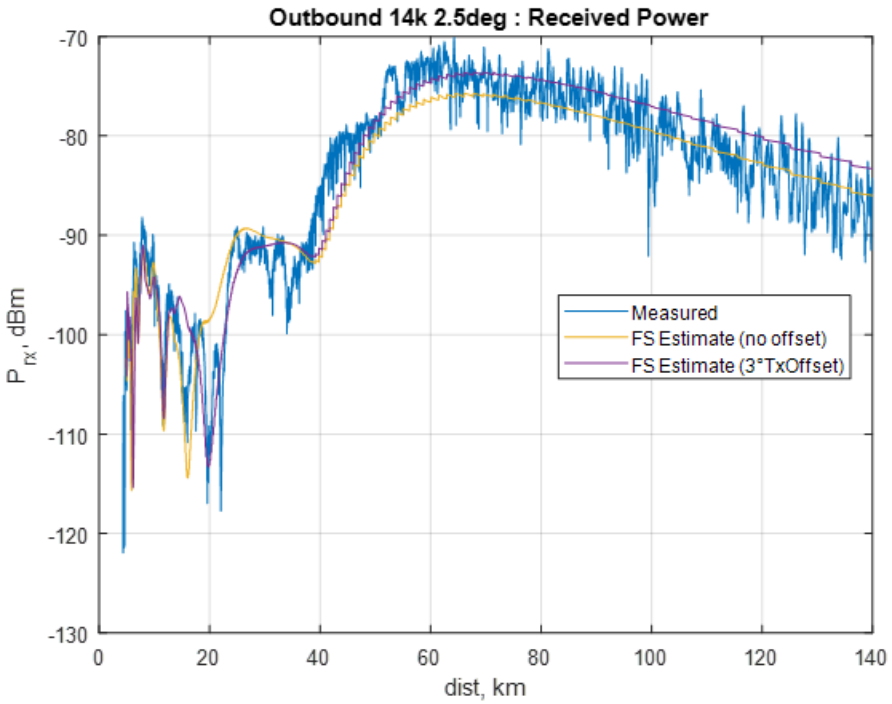

Figure 3.9. Received power versus link distance comparing estimates with and without offset.

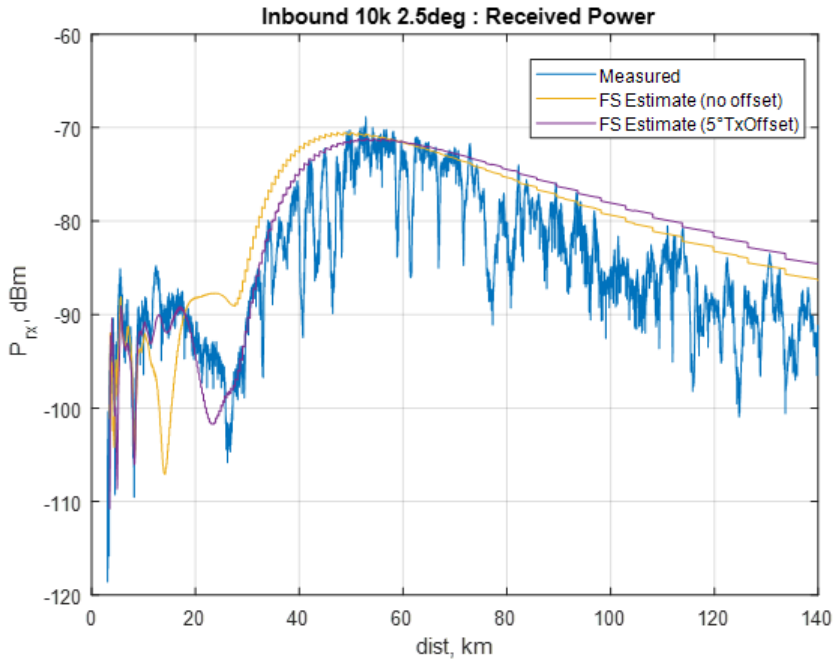

Figure 3.10. Received power versus link distance comparing estimates with and without offset.

Chapter 4. Path Loss Models

In this chapter, the theoretical path loss models are described. The equations used for free-space path loss and two-ray path loss are shown. Readers are reminded how atmospheric attenuation, here in the form of fog, and atmospheric refraction modify results. Lastly, log-distance path loss equations are presented. These models are widely used in terrestrial and other channels, and provide a parameter describing goodness of fit to the measured data.

4.1 Free-space Model

The free-space path loss definition is given in equation (4.1), in dB, where r is the link distance and λ is the wavelength, which at 14.25 GHz is 0.0210 meters.

$$L_{fs} = 20 \log_{10} \left(\frac{4\pi r}{\lambda} \right) \tag{4.1}$$

4.2 Two-Ray Model

The highly directional parabolic antenna used in our experiments requires care when determining the 2-ray channel model. Except at large link distances, the reflected component will not have the same antenna gain as the line-of-sight component. This is illustrated in Figure 4.1. To determine the path loss, power density is used to find the ratio between power transmitted and power received. This ratio will be compared to the standard link budget equation, which will allow for a term to be found for 2-ray path loss.

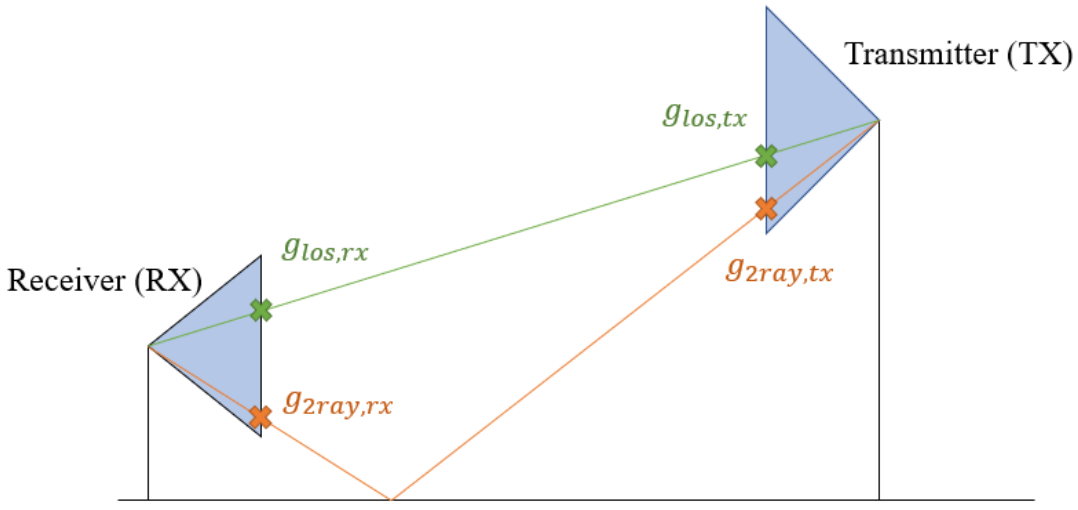

Figure 4.1 Antenna gains formed from line-of-sight (LOS) beam and reflected (2ray) beam.

At the surface of sphere with radius r, containing an antenna at the center, transmitting a power level p (in watts), is a power density p_d, which can be written as (4.2),

$$p_d = \frac{p}{4\pi r^2}. \tag{4.2}$$

Equation (4.2) can be rearranged to solve for transmit power p_t, shown in (4.3),

$$p_t = p_{d,tx} 4\pi r^2. \tag{4.3}$$

Power density can also be determined by the cross product of the electric field and the magnetic field. In a normalized system, the magnitude of the power density can be found as the electric field squared.

$$p_d = E \times H \tag{4.4}$$

$$|H| = \frac{|E|}{Z_0} = |E|_{Z_0=1} \tag{4.5}$$

$$p_d = |E|^2 \tag{4.6}$$

The power density at the transmitter can be defined as (4.7):

$$p_{d,tx} = |E_0|^2. \tag{4.7}$$

The transmitter power can then be written as equation (4.8):

$$p_t = |E_0|^2 4\pi r^2. \tag{4.8}$$

After defining effective antenna area as equation (4.9), the received power can be written as (4.10),

$$A_e = \frac{\lambda^2}{4\pi}, \tag{4.9}$$

$$p_r = p_{d,rx} A_e. \tag{4.10}$$

The electric field at the receiver can be written as a line-of-sight (LOS) component with a reflected component modified by the gains of the antennas (square roots of the gains are used here, since the gains are typically specified as linear power gains),

$$E_r = E_0\left[\sqrt{g_{tx,los} g_{rx,los}} + \sqrt{g_{tx,2ray} g_{rx,2ray}}\Gamma e^{-j\Delta\phi}\right] \tag{4.11}$$

where Γ is the reflection coefficient and $\Delta\phi$ is the phase difference between the LOS and reflected components, computed using the difference in path lengths, which can be calculated using geometry, e.g., [6].

The power density at the receiver can be written as

$$p_{d,rx} = E_r^2. \tag{4.12}$$

Equation (4.12) can be used in (4.10) to yield (4.13) for received power:

$$p_r = \frac{E_r^2 \lambda^2}{4\pi}. \tag{4.13}$$

The ratio of received power to transmit power can then be written as (4.14):

$$\frac{p_r}{p_t} = \left(\frac{\left(\left[\sqrt{g_{tx,los} g_{rx,los}} + \sqrt{g_{tx,2ray} g_{rx,2ray}} \Gamma e^{-j\Delta\phi} \right] \lambda \right)}{4\pi r} \right)^2. \tag{4.14}$$

Rewriting this equation in logarithmic form yields (4.15):

$$P_{r,dBm} - P_{t,dBm} = 20 \log_{10} \left(\frac{\left(\left[\sqrt{g_{tx,los} g_{rx,los}} + \sqrt{g_{tx,2ray} g_{rx,2ray}} \Gamma e^{-j\Delta\phi} \right] \lambda \right)}{4\pi r} \right). \tag{4.15}$$

In order to compare the 2-ray channel with the free-space attenuation path loss, the line-of-sight gains are factored out of the right side of equation (4.15), to yield

$$P_{r,dBm} - P_{t,dBm} = 20 \log_{10} \left(\frac{\lambda}{4\pi r} \sqrt{g_{tx,los} g_{rx,los}} \left[1 + \sqrt{\frac{g_{tx,2ray} g_{rx,2ray}}{g_{tx,los} g_{rx,los}}} \Gamma e^{-j\Delta\phi} \right] \right). \tag{4.16}$$

The right side of equation (4.16) can be expanded via logarithm addition identities to give (4.17):

$$20 \log_{10} \left(\sqrt{g_{tx,los} g_{rx,los}} \right) + 20 \log_{10} \left(\frac{\lambda}{4\pi r} \left[1 + \sqrt{\frac{g_{tx,2ray} g_{rx,2ray}}{g_{tx,los} g_{rx,los}}} \Gamma e^{-j\Delta\phi} \right] \right). \tag{4.17}$$

With uppercase G denoting the antenna gain in decibels, (4.17) can be rewritten as (4.18).

$$P_r - P_t = G_{tx,los} + G_{rx,los} + 20 \log_{10} \left(\frac{\lambda}{4\pi r} \left[1 + \sqrt{\frac{g_{tx,2ray} g_{rx,2ray}}{g_{tx,los} g_{rx,los}}} \Gamma e^{-j\Delta\phi} \right] \right). \tag{4.18}$$

The typical link budget, defined in equation (3.1), can be rewritten to solve for loss, which is shown in (4.19):

$$L = -P_r + P_t + G_{tx} + G_{rx}. \tag{4.19}$$

Finally, the path loss for the 2-ray channel can be written as (4.20):

$$L_{2ray} = -20\log_{10}\left(\frac{\lambda}{4\pi r}\left[1 + \sqrt{\frac{g_{tx,2ray}g_{rx,2ray}}{g_{tx,los}g_{rx,los}}}\Gamma e^{-j\Delta\phi}\right]\right). \tag{4.20}$$

4.3 Atmospheric Attenuation

As mentioned in chapter 3, hydro-meteor attenuation from the presence of fog occurred on the flight test days. The cloud attenuation constant used in the path loss models is α=0.022374 dB/km (calculated in section 3.4). This attenuation can be added to that of any path loss model, via $L_{fog}(d) = \alpha d$ where d is in km.

4.4 Atmospheric Refraction

Also mentioned in chapter 3, atmospheric refraction is taken into account in path loss models in the form of the effective earth radius modifier k. Table 4.1 summarizes effective modifier values. The value depends on height, so there are values given for each flight track altitude.

Table 4.1 Atmospheric refraction constants for given aircraft altitudes.

Flight Altitude (ft)	***k***
3,000	1.3461
10,000	1.2835
14,000	1.2538

4.5 Log-distance Path Loss Models

For the purposes of comparison, log-distance equations have been fit to measured data. The equations take the form defined by (4.21), with L in dB.

$$L(d) = PL_0 + n10\log_{10}(d) + X\,. \tag{4.21}$$

These fits employ the common least-squares technique, which yields the straight line that minimizes the sum of the squared error between the measurements and the fit line. The variable X is a normally (Gaussian) distributed random variable, and its standard deviation—which is the measure of goodness of fit—is given in Table 4.2, along with the path loss exponent n and the offset PL_0. This table constitutes the path loss models for each of the individual flight tracks. This table also includes a loss value we term ΔL_{max}, which is the maximum difference between measured path loss and the free-space path loss. This value can be used to highlight the "worst case" path loss beyond what the free-space loss predicts.

Table 4.2 Parameters for log-distance path loss equations for given flight tracks.

Flight Track (Offset, In/Out-bound, Altitude (ft), Inclination, Antenna)	**Path Loss Exponent**	**Offset**	**Std Dev (dB)**	**ΔL_{max} (dB)**
6ºTXoffset Inbound 3k 5deg: Parabolic	1.94	119.06	2.48	22.78
6ºTXoffset Inbound 3k 5deg: V. Horn	2.23	110.35	1.86	7.78
6ºTXoffset Inbound 3k 5deg: H. Horn	2.60	106.17	3.67	27.96
7ºTXoffset Inbound 10k 5deg: Parabolic	2.47	110.53	3.03	28.28
7ºTXoffset Inbound 10k 5deg: V. Horn	2.56	105.48	2.98	27.40
7ºTXoffset Inbound 10k 5deg: H. Horn	2.99	97.10	3.88	23.42
6ºTXoffset Inbound 14k 5deg: Parabolic	2.42	110.88	2.95	24.66
6ºTXoffset Inbound 14k 5deg: V. Horn	2.60	104.29	2.86	22.97
6ºTXoffset Inbound 14k 5deg: H. Horn	3.26	91.79	4.89	24.73
-4ºTXoffset Outbound 3k 5deg: Parabolic	1.52	120.82	3.18	31.51
-4ºTXoffset Outbound 3k 5deg: V. Horn	1.75	112.09	2.50	26.90
-4ºTXoffset Outbound 3k 5deg: H. Horn	1.99	107.36	4.37	18.19
1ºTXoffset Outbound 10k 5deg: Parabolic	2.26	112.25	1.92	17.08
1ºTXoffset Outbound 10k 5deg: V. Horn	2.32	107.61	1.68	11.21
1ºTXoffset Outbound 10k 5deg: H. Horn	2.56	103.42	4.33	27.02
2ºTXoffset Outbound 14k 5deg: Parabolic	2.00	115.94	1.93	15.53
2ºTXoffset Outbound 14k 5deg: V. Horn	2.24	108.53	1.95	12.24
2ºTXoffset Outbound 14k 5deg: H. Horn	2.54	103.04	5.13	30.06

For the receiver at a 5 degree inclination, the minimum value for path loss exponent was found to be 1.52, which is from the highly directional parabolic antenna during an outbound flight at the lowest altitude. Almost all of the lowest altitude (3000 ft) flights resulted in the smallest path loss exponents. Although the 10,000 ft and 14,000 ft altitude flights had link distances up to 120 km, the 3000 ft altitude flights only ranged to 65 km. The largest path loss exponent (for a 5 degree receiver inclination angle) was found to be 3.26, which pertains to the horizontally polarized horn antenna for an inbound flight at the highest altitude. This is significantly larger than the free-space path loss exponent of 2 and is likely due to additional losses introduced by being cross-polarized with respect to the test signal. For the same reason, the standard deviations of the fits for the cross-polarized horn antenna are larger than all other fitted curves for all inclination angles. The standard deviation of the vertical horn is, in general, smaller than that for the parabolic antenna because the measurements were practically always made inside the main beam of the horn antenna. The parabolic antenna had an extremely small beamwidth (about 2.5 degrees), which allowed for segments of the flight path to be *outside* the main lobe. The receiver gains are then more prone to larger fluctuation when the parabolic antenna is used, compared to the horn antenna. When comparing offset values (PL_0), it can be seen that for the same type of antenna, lower offsets typically occur at higher flight altitudes. We do not attribute much of physical significance to the offsets. Somewhat surprising is that the horizontally polarized horn antenna yields the lowest offset for a given flight track when compared to the vertical horn and parabolic antennas. Comparing the averages of inclination angles, as the receiver inclination angle increases, path loss exponents decrease,

while offsets increase for the parabolic and vertically polarized horn antennas (co-polarized test antennas).

Figures 4.2 – 4.4 show various inbound and outbound flight path loss versus distance plots for the parabolic, vertical horn, and horizontal horn antennas. Most of the plots have a log-distance curve that has a path loss exponent of approximately two, which is equal to the free-space path loss exponent. Figure 4.2 shows that the free-space path loss estimate at small distances overestimates loss for the vertical horn antenna, but at larger link distances (beyond 10 km) the free-space estimate is in better agreement with measured data.

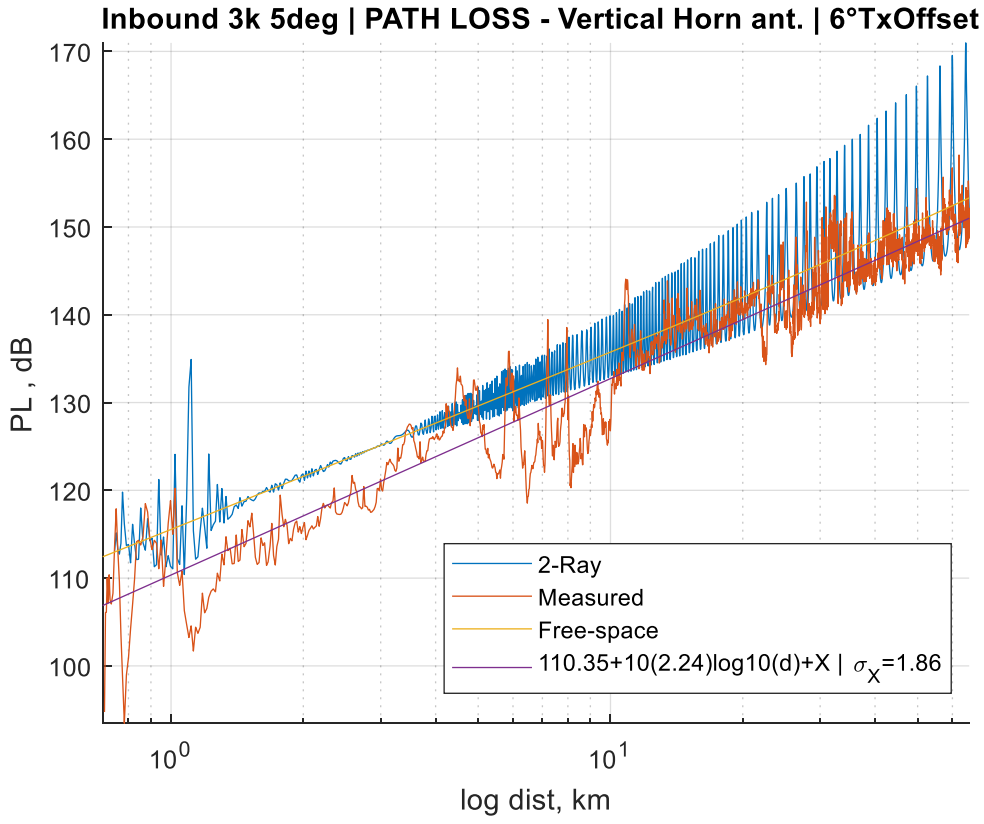

Figure 4.2 Path loss for an inbound flight track with the vertical horn antenna.

Figure 4.3 shows a better fit at all link distances when comparing the log-distance fitted curve to the free-space and 2-ray path loss estimates. The large loss spike around 43 km occurs for both the parabolic and vertically polarized horn antenna on this flight track (inbound 10,000 ft and 5 degree inclination), but not for the horizontally polarized horn antenna. Because this spike is much more than 9 dB and persists for over 1 km, it is unlikely this occurred from only destructive interference from a reflection.

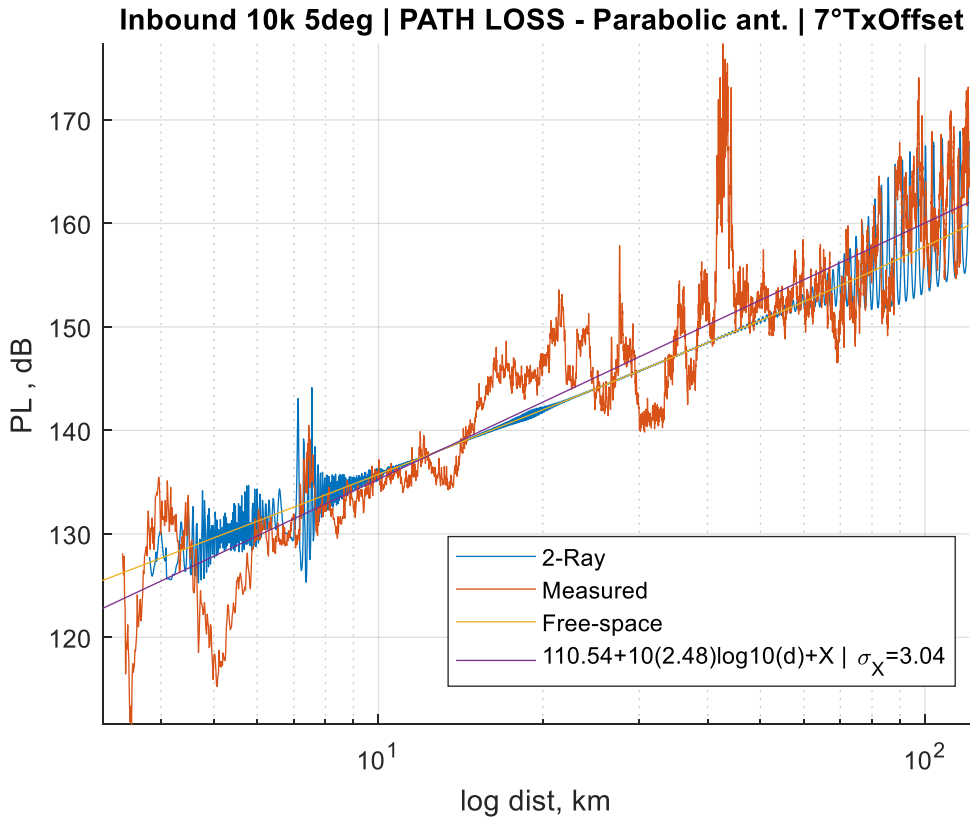

Figure 4.3 Path loss for an inbound flight track with the parabolic antenna.

Figure 4.4 shows the horizontal (cross-polarized) horn antenna path loss curves. The free-space and 2-ray curves again overestimate the loss, with the overestimate amount decreasing at longer link distances.

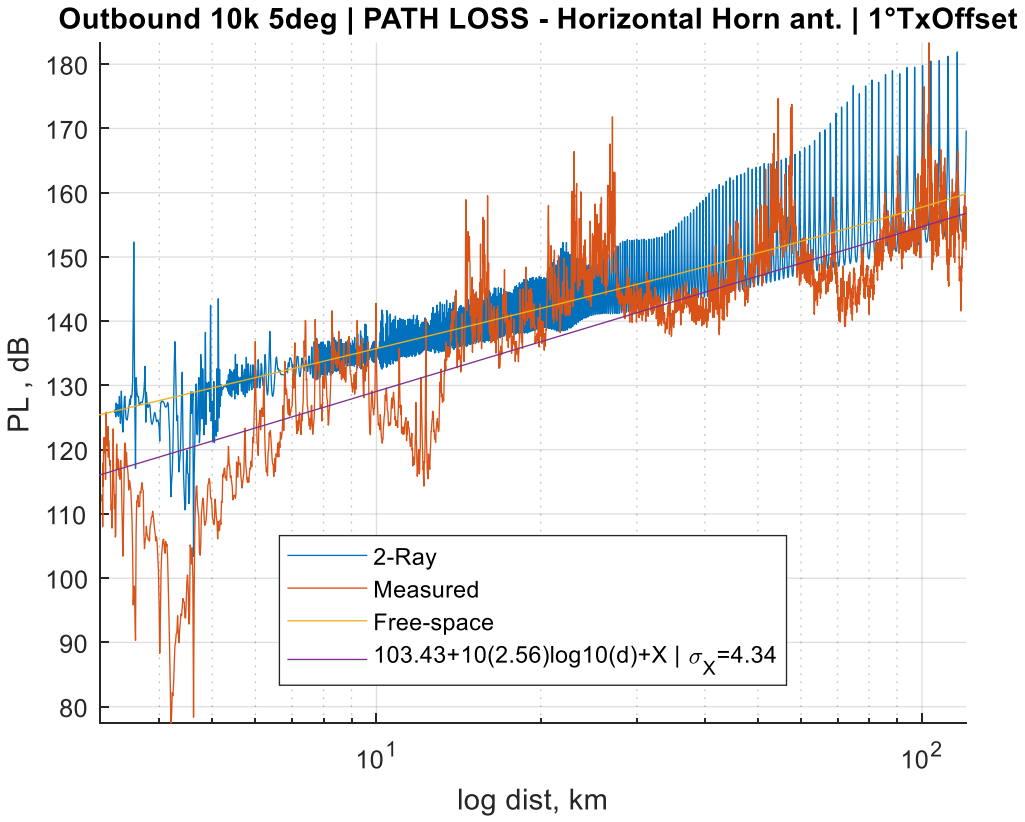

Figure 4.4 Path loss for an outbound flight track with the horizontal horn antenna.

Chapter 5. Conclusion

5.1 Summary

In this thesis a rationale and motivation was presented for measuring and quantitatively modeling the Ku-band AG channel. Previous works were examined for this frequency band and found to focus primarily on ground-to-satellite links. To use air-to-satellite communication and control for unmanned aerial systems, the air-to-ground channel needs to be quantified for use in determining potential interference with existing terrestrial infrastructure that uses this band.

The methodology of the tests was described in chapter two, including examination of the several antennas used in the tests. Chapter three contains test results in the form of power measurements with respect to distance. A program was written to convert aircraft GPS measurement data into distances, enabling the received power to be expressed as a function of distance. Additionally, in this MATLAB program, a free-space model and a two-ray model were implemented to predict estimated received power. These models were refined for this environment by the inclusion of atmospheric attenuation (due to fog) and atmospheric refraction. Chapter four contains the path loss models used, and in this chapter comparison to the popular log-distance models was made. When compared to the log-distance equation fit to measured data, it was found that the free-space and two-ray calculations generally overestimated loss. For a 5 degree receiver antenna inclination, the measured data from co-polarized antennas were found to have path loss exponents close to

that of free-space (value of 2). As inclination angle approaches the horizon boresight (0 degrees), the path loss exponents increased and the path loss offsets (PL_0) decreased for co-polarized antennas.

5.2 Future Work

Future work would include modeling the air-to-satellite link in the Ku-band, to enable estimation of aircraft power levels, which of course directly affect any air-ground interference. Pursuing a more rigorous and accurate air-ground channel model development, to account for *all* the effects seen in the measured results, would be of value. Also, examination into other antenna mounting locations for the AG Ku-band channel could be undertaken. In addition to mounting locations, other antennas mounted to the aircraft would be of interest. The antenna used was not a true omnidirectional antenna, as it contained several deep nulls in the gain pattern (see Figure 2.5). This necessitated the use of antenna angular offset to account for aircraft pitch in gain estimates. Using an antenna that is a true omnidirectional antenna, or at least has a pattern without significant nulls, could help decouple the influence of antenna gain and channel losses. Channel modeling with a higher bandwidth, and actual dual polarization, would also be of interest.

Tests could be conducted with different weather effects examined, as well. The Ku-band is known to suffer from hydro-meteor attenuation, so it could be of interest to characterize the channel in poor weather conditions. Finally modeling the Ku-band in other environments may be interesting. As the test environment was over a generally hilly area, dense cities and over seawater could have different characteristics.

References

[1] D. W. Matolak, "Ku-Band AG Channel Measurement," European Conference on Antennas and Propagation (EuCAP), London, UK, 9-13 April 2018.

[2] S. Scalise, H. Ernst and G. Harles, "Measurement and Modeling of the Land Mobile Satellite Channel at Ku-band," *IEEE Transactions on Vehicular Technology*, vol. 57, no. 2, pp. 693-703, 2008.

[3] S. Rougerie and B. Montenegro-Villacieros, "Mobile Satellite Propagation Channels for Ku and Ka band", European Conference on Antennas and Propagation (EuCAP), Davos, Switzerland, 10-15 April 2016.

[4] D. Matolak and R. Sun, "Air-Ground Channels for UAS: Summary of Measurements and Models for L- and C-band," AIAA/IEEE Integrated Communications Navigation and Surveillance (ICNS) Conference, Herndon, VA, USA 19-21 April 2016.

[5] C. Levis, J. Johnson and F. Teixeira, *Radiowave Propagation*, Hoboken, NJ: John Wiley & Sons, Inc., 2010.

[6] International Telecommunications Union, ITU-R Recommendation P. 530-17, "Propagation data and prediction methods required for the design of terrestrial line-of-sight systems," 2017.

[7] International Telecommunications Union, ITU-R Recommendation P.676-11, "Attenuation by atmospheric gases," 2016.

[8] International Telecommunications Union, ITU-R Recommendation P.834-4, "Effects of tropospheric refraction on radiowave propagation," 2003.

[9] International Telecommunications Union, ITU Report, "Reflection from the surface of the Earth (Report 1008-1)," 1990.

[10] K. Shalkhauser, "Figure/photo courtesy of NASA GRC".

[11] "Product specification for Commscope VHLP2-15-1WH/B," Commscope, 2018. [Online]. Available: https://www.commscope.com/catalog/antennas/product_details.aspx?id=52671.

[12] D. W. Matolak, "AG Channel Measurements & Modeling: Initial Analysis & Flight Test Planning," (Report #2) NASA Grant #NNX12AD53G 2012.

[13] International Telecommunications Union, ITU-R Recommendation P.453-13, "The radio refractive index: its formula and refractivity data," 2017.

[14] C. Phillips, D. Sicker and D. Grunwald, "A Survey of Wireless Path Loss Prediction and Coverage Mapping Methods," *IEEE Communications Surveys & Tutorials,* vol. 15, no. 1, pp. 255-269, 2013.

APPENDIX A: Path loss plots for all flight tracks sorted by inclination angle

In this index, readers will find plots of path loss which include measured, free-space, two-ray, and log-distance fit for all receiver inclination (elevation) angles and all flight tracks. Plots are of horizontal and vertical horn antennas and parabolic antennas are separated for readability. Titles to plots include angular offset used and describe which flight track the plot represents.

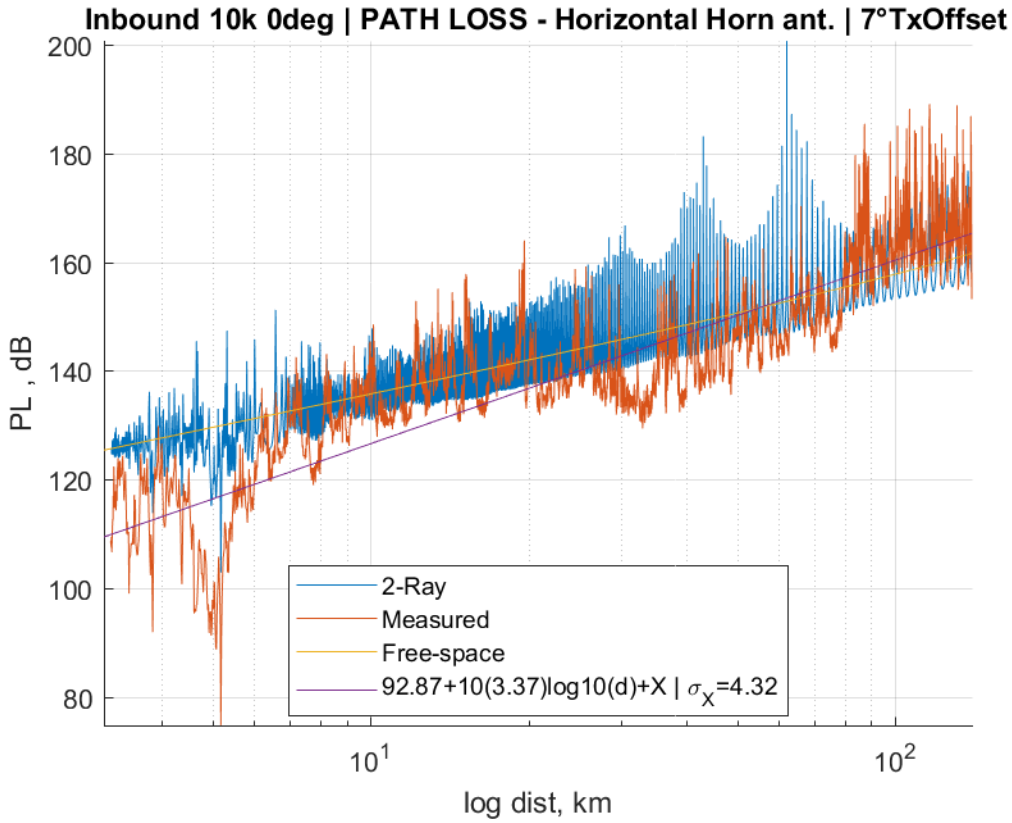

Figure A.1 Path loss for an inbound flight track with the horizontal horn antenna.

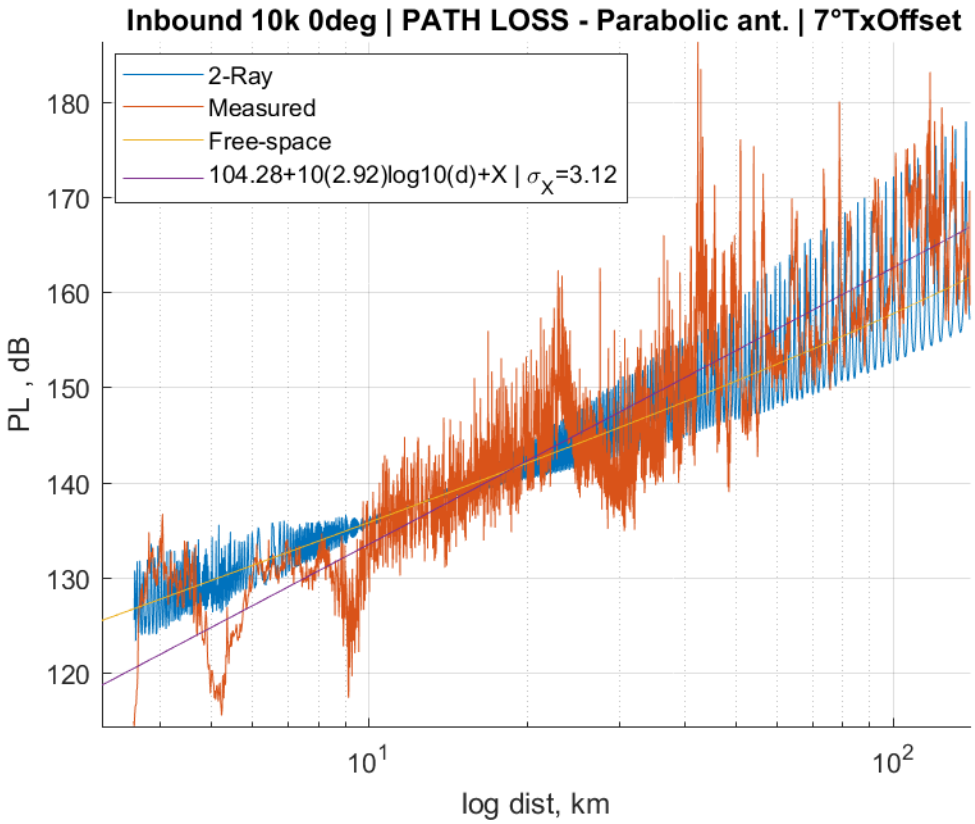

Figure A.2 Path loss for an inbound flight track with the parabolic antenna.

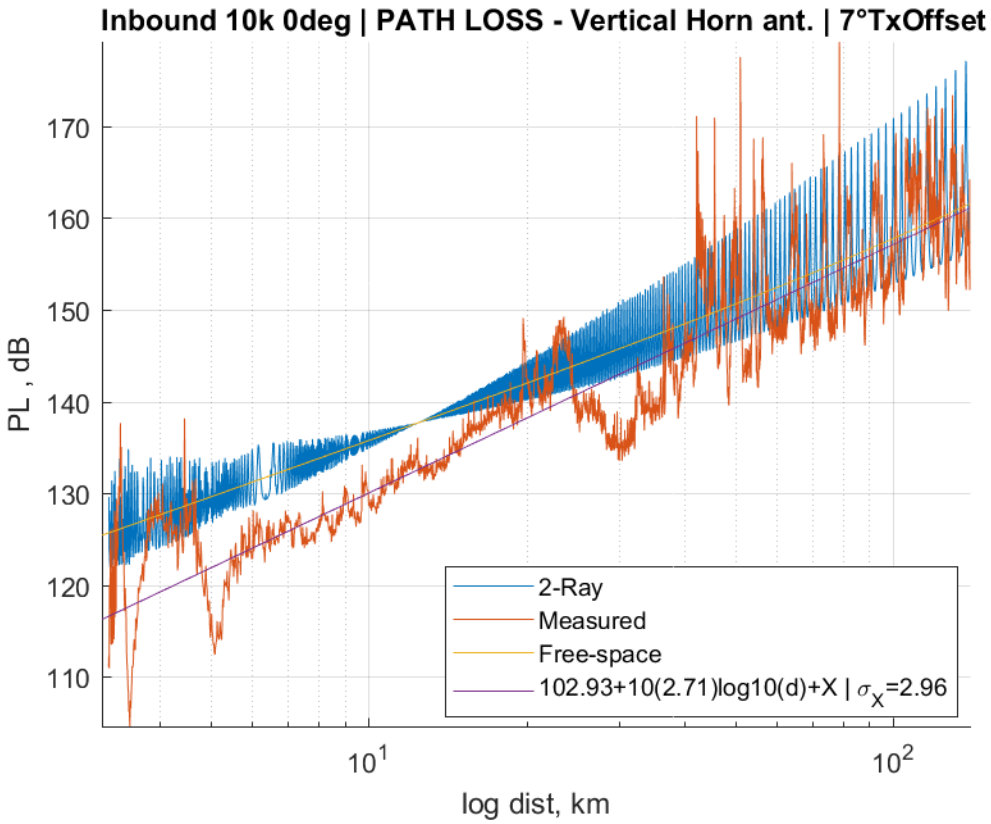

Figure A.3 Path loss for an inbound flight track with the vertical horn antenna.

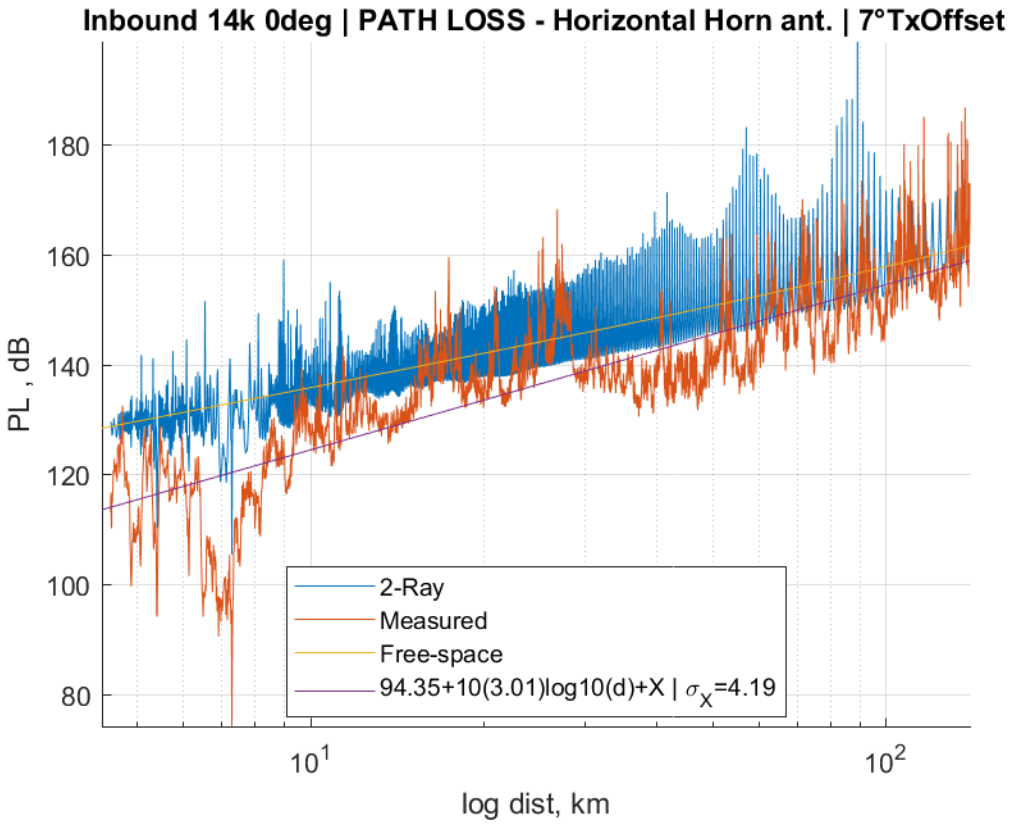

Figure A.4 Path loss for an inbound flight track with the horizontal horn antenna.

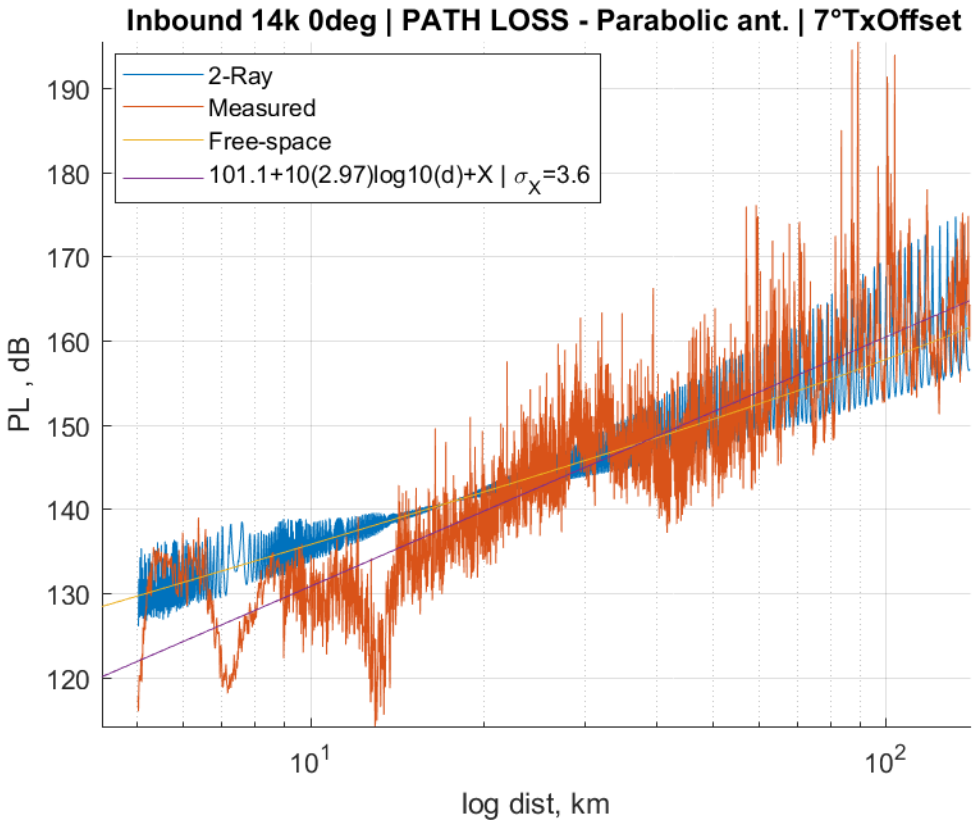

Figure A.5 Path loss for an inbound flight track with the parabolic antenna.

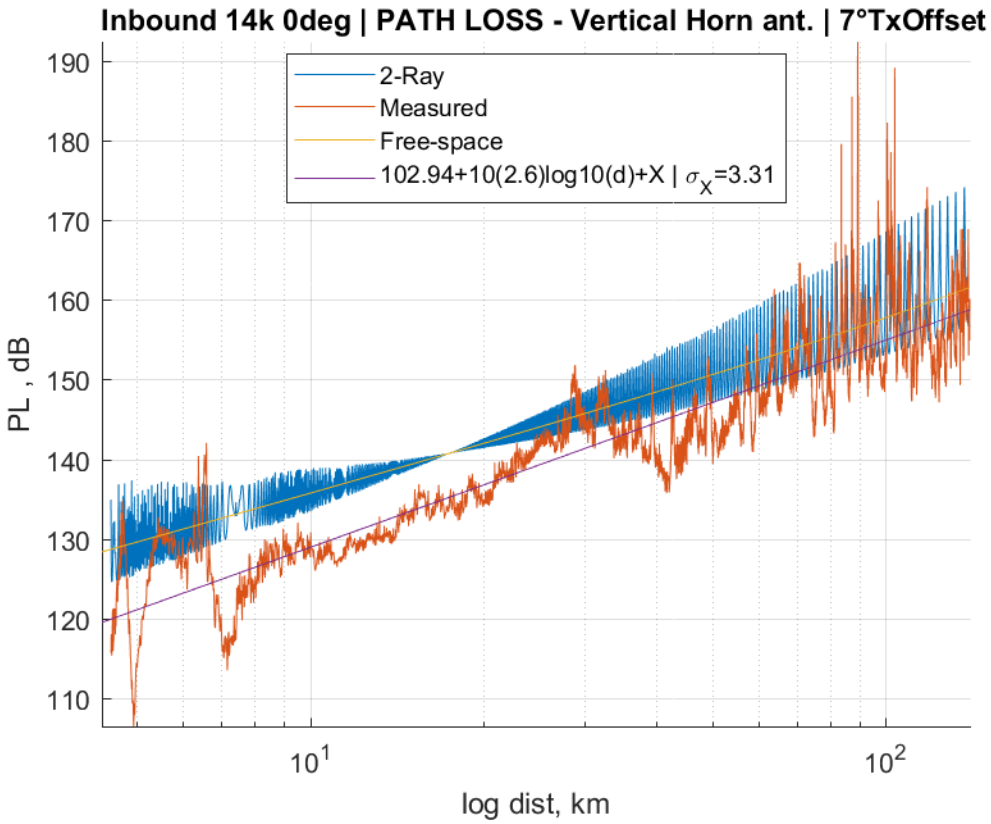

Figure A.6 Path loss for an inbound flight track with the vertical horn antenna.

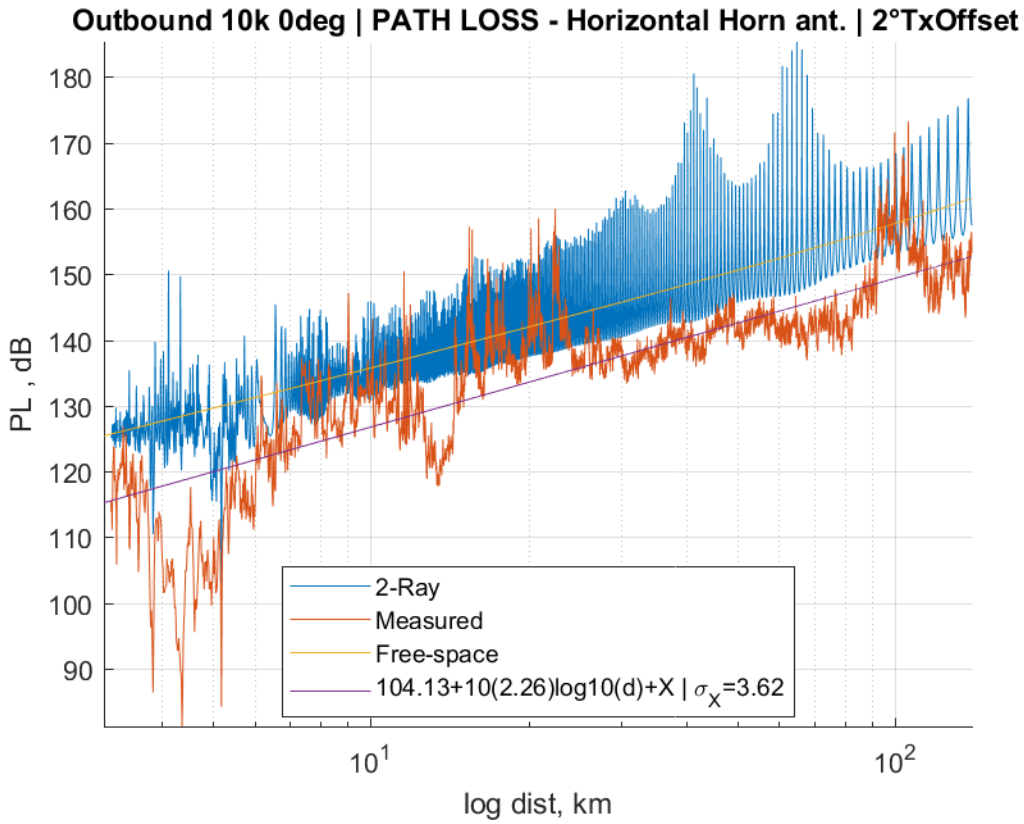

Figure A.7 Path loss for an outbound flight track with the horizontal horn antenna.

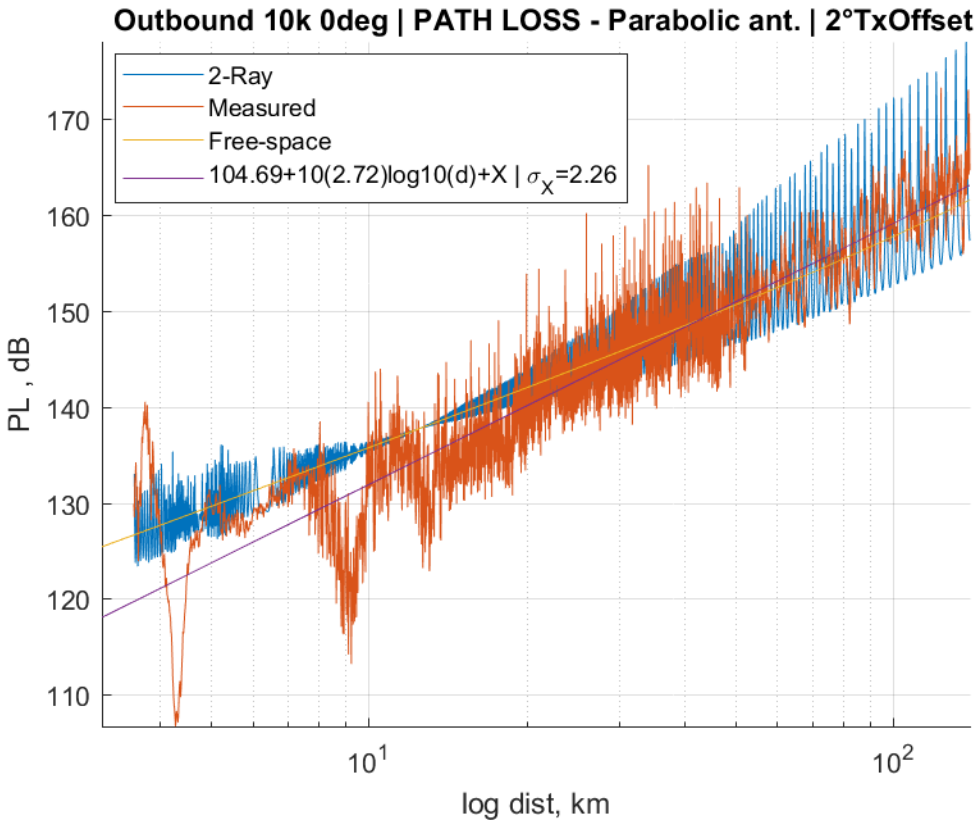

Figure A.8 Path loss for an outbound flight track with the parabolic antenna.

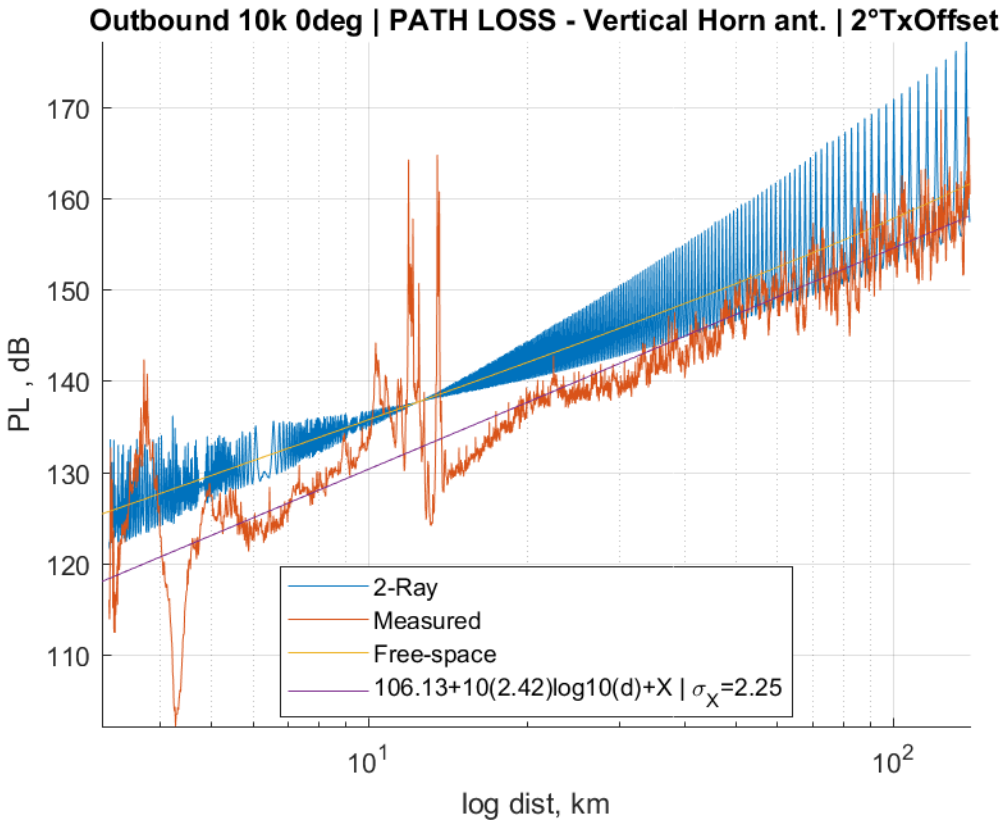

Figure A.9 Path loss for an outbound flight track with the vertical horn antenna.

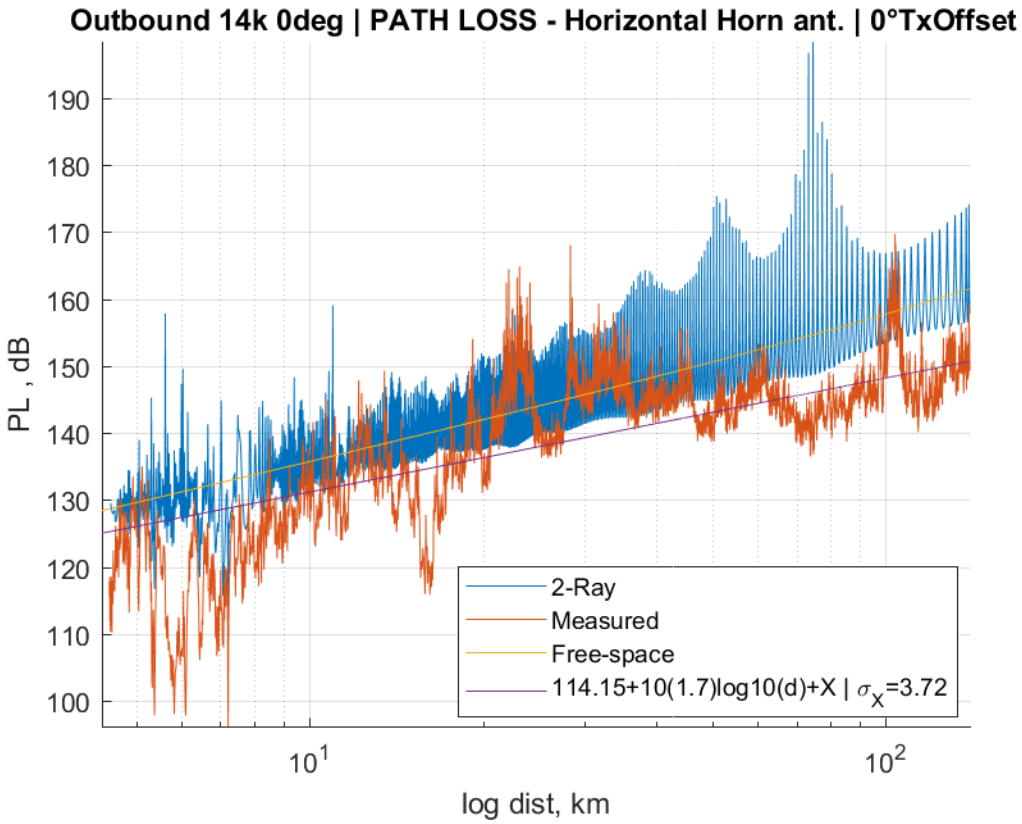

Figure A.10 Path loss for an outbound flight track with the horizontal horn antenna.

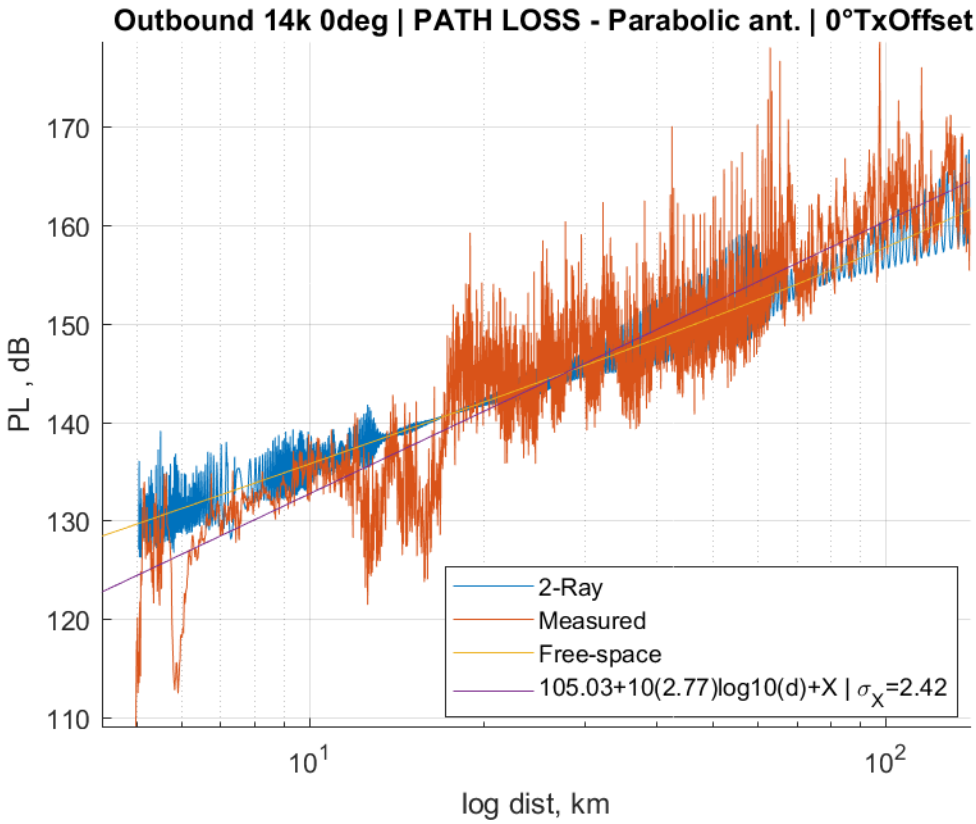

Figure A.11 Path loss for an outbound flight track with the parabolic antenna.

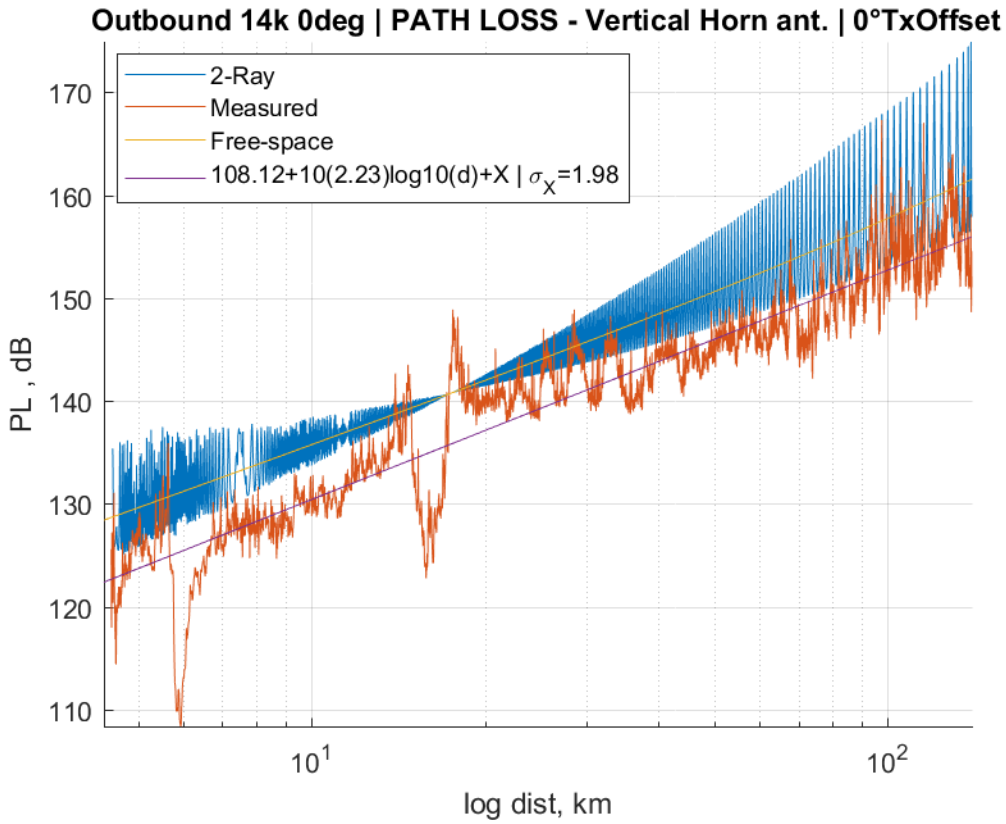

Figure A.12 Path loss for an outbound flight track with the vertical horn antenna.

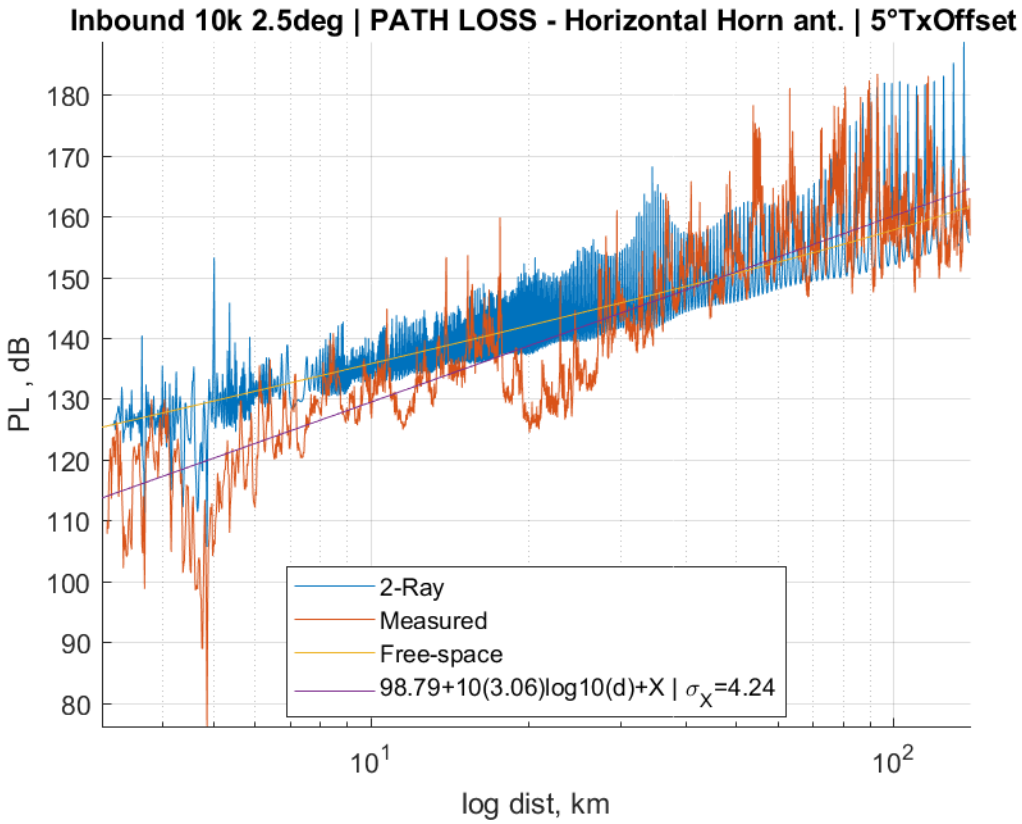

Figure A.13 Path loss for an inbound flight track with the horizontal horn antenna.

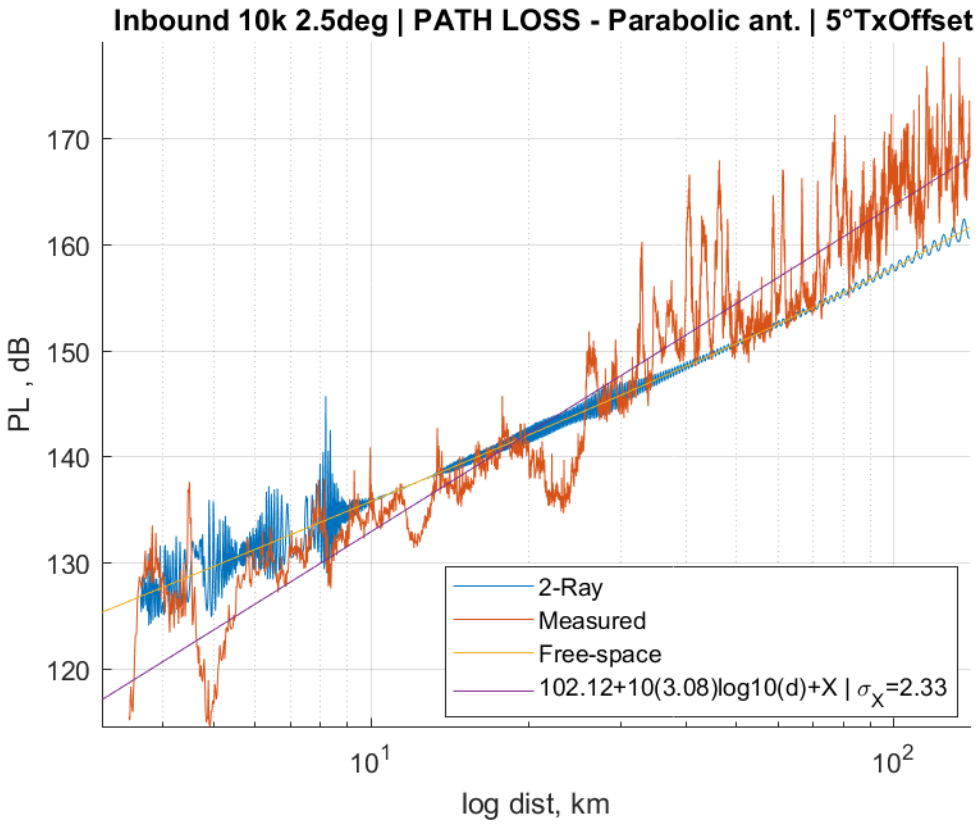

Figure A.14 Path loss for an inbound flight track with the parabolic antenna.

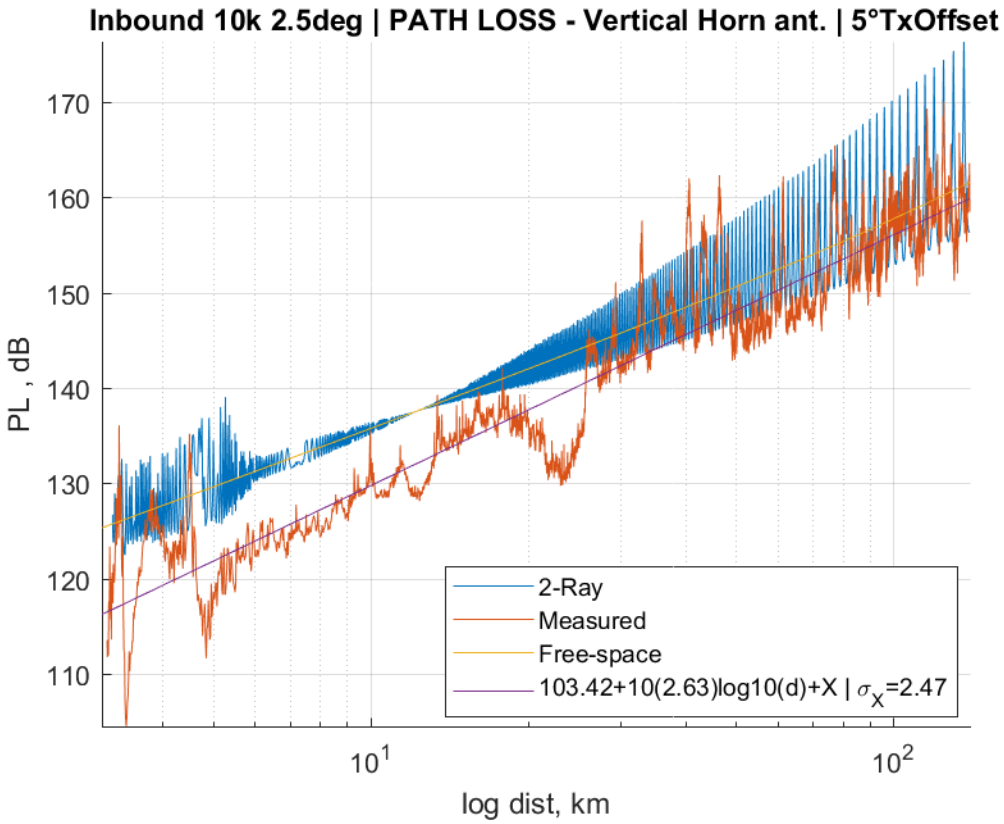

Figure A.15 Path loss for an inbound flight track with the vertical horn antenna.

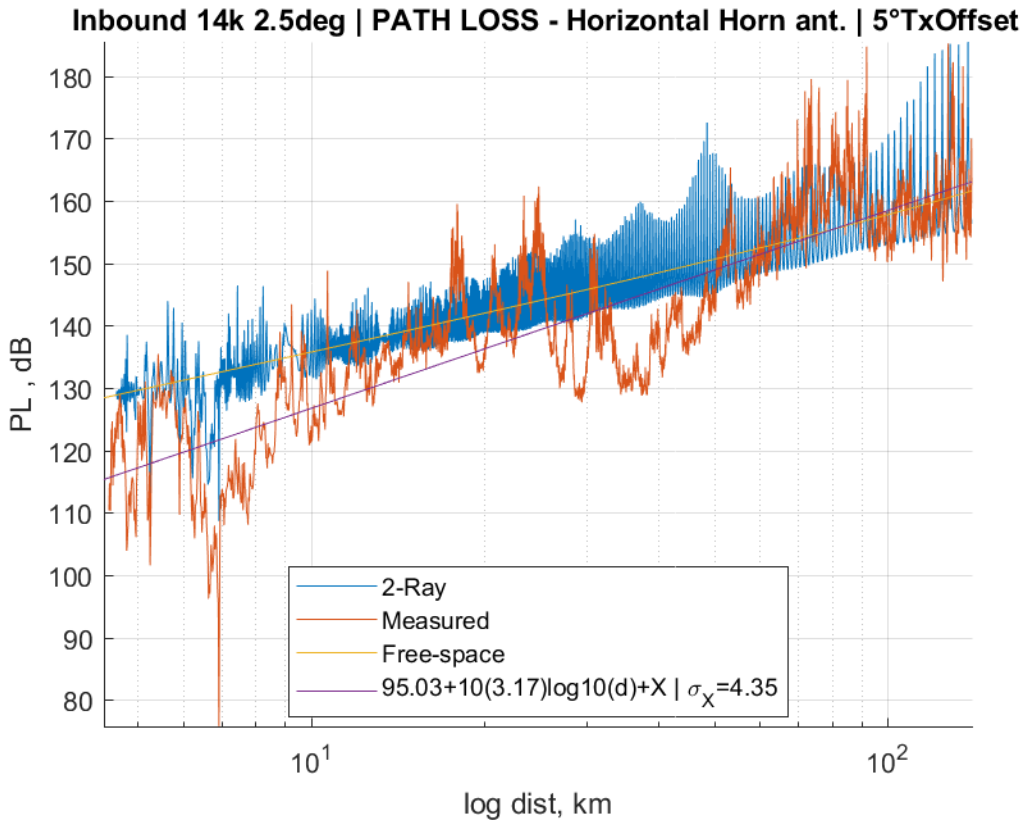

Figure A.16 Path loss for an inbound flight track with the horizontal horn antenna.

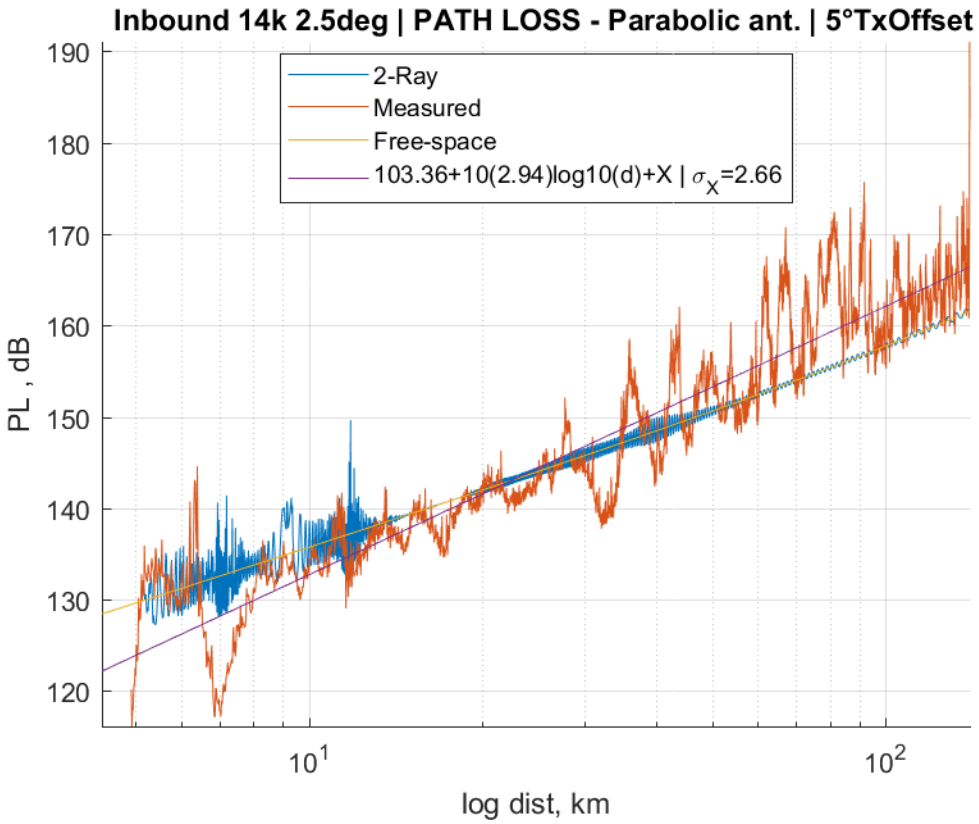

Figure A.17 Path loss for an inbound flight track with the parabolic antenna.

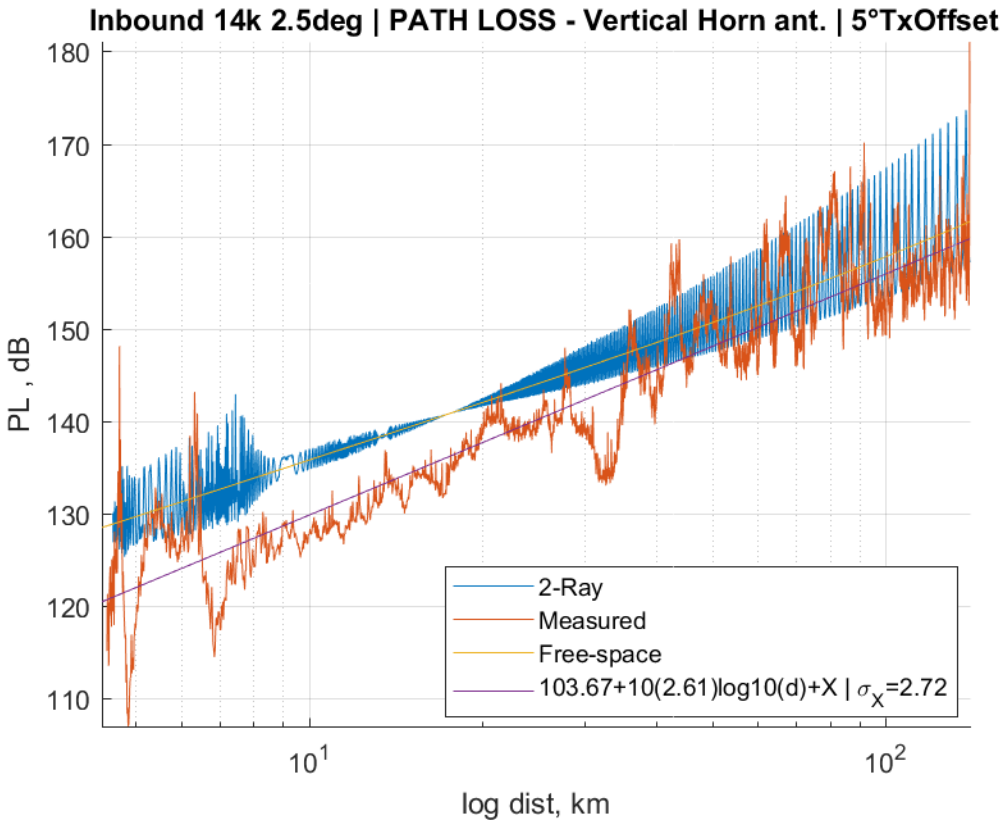

Figure A.18 Path loss for an inbound flight track with the vertical horn antenna.

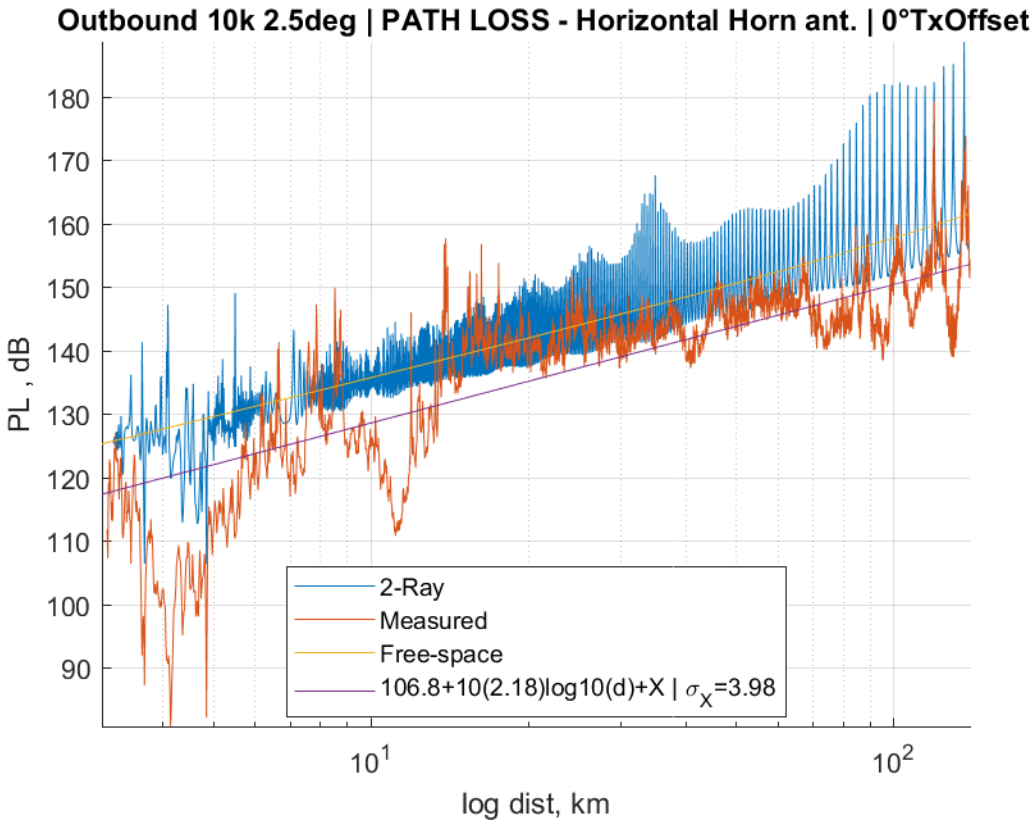

Figure A.19 Path loss for an outbound flight track with the horizontal horn antenna.

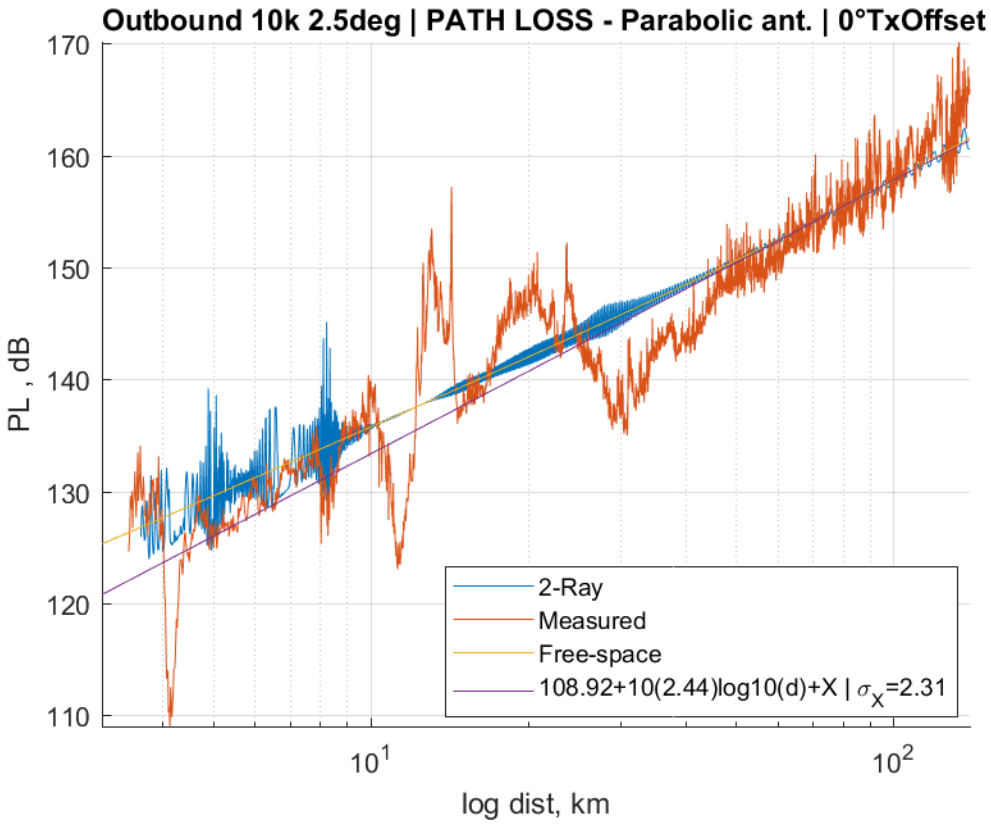

Figure A.20 Path loss for an outbound flight track with the parabolic antenna.

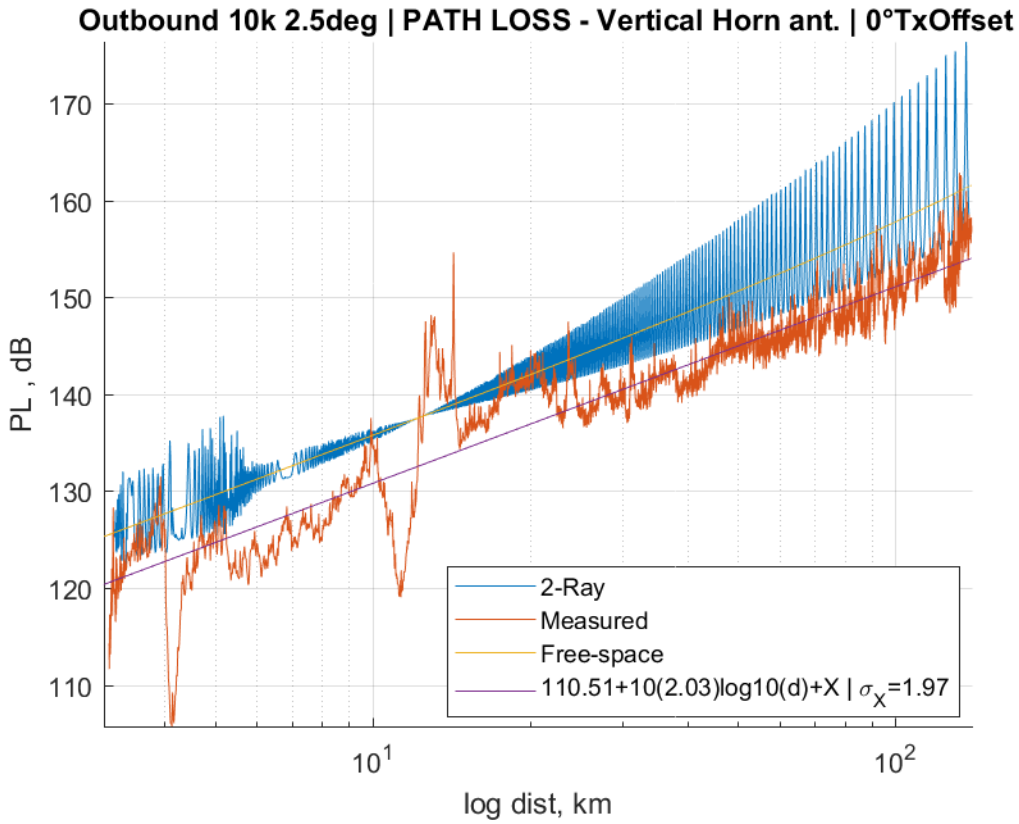

Figure A.21 Path loss for an outbound flight track with the vertical horn antenna.

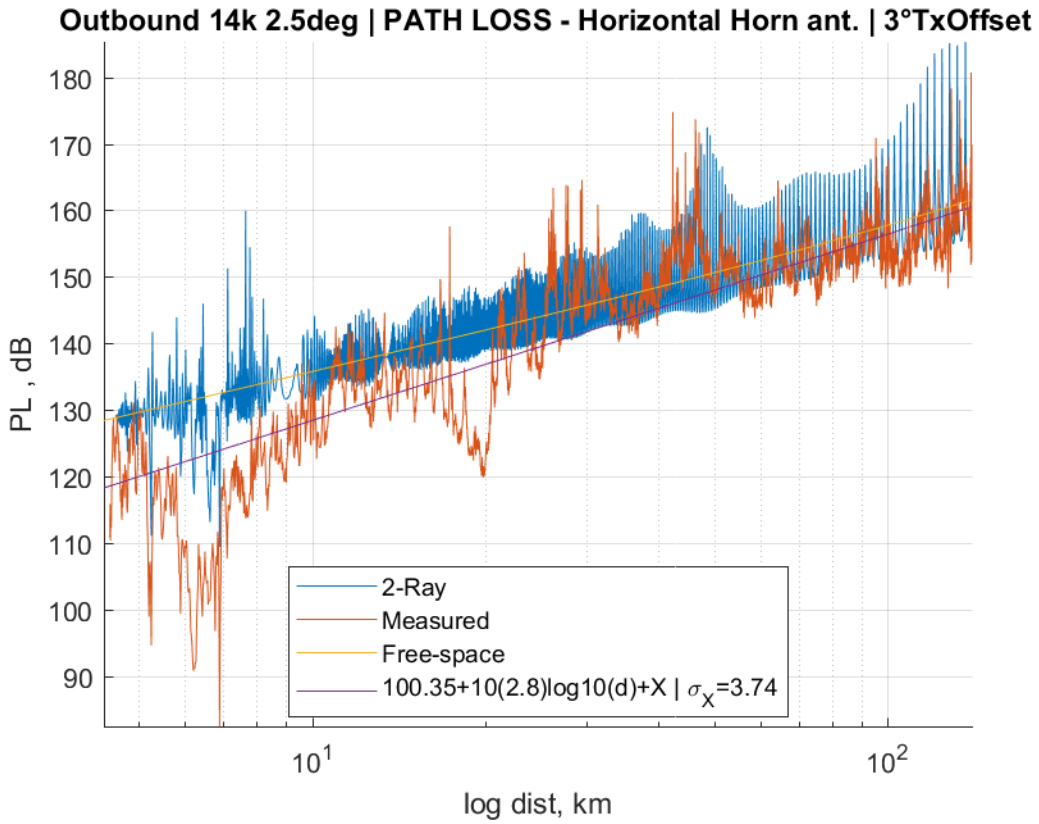

Figure A.22 Path loss for an outbound flight track with the horizontal horn antenna.

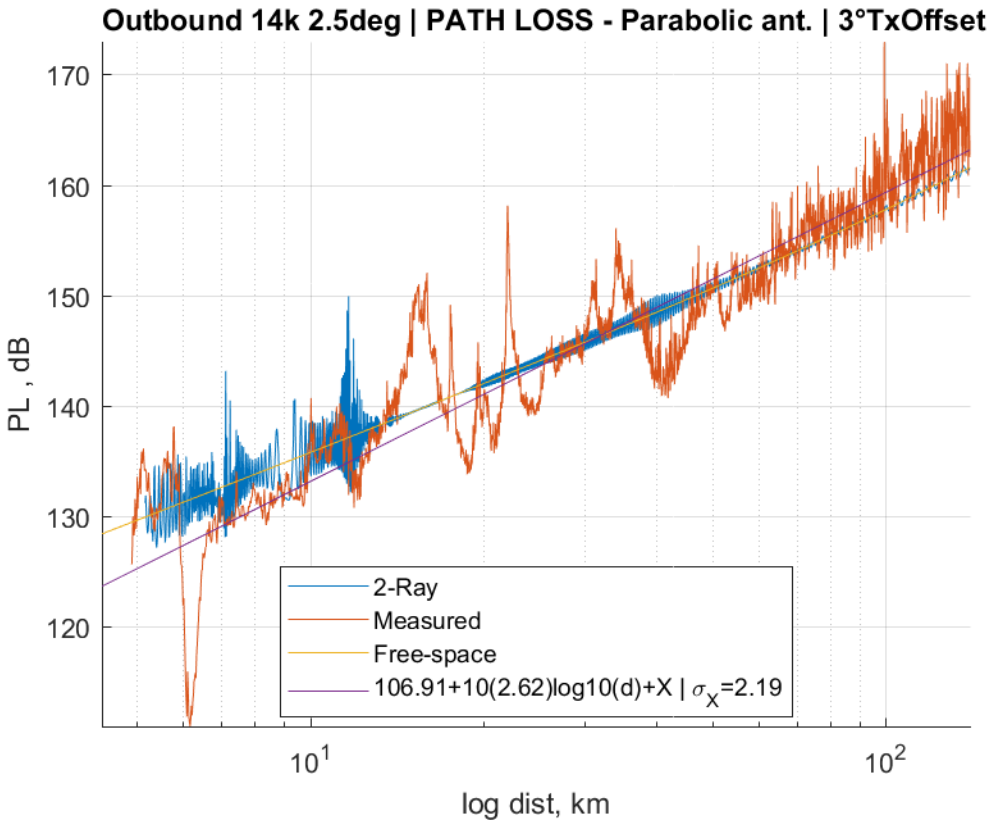

Figure A.23 Path loss for an outbound flight track with the parabolic antenna.

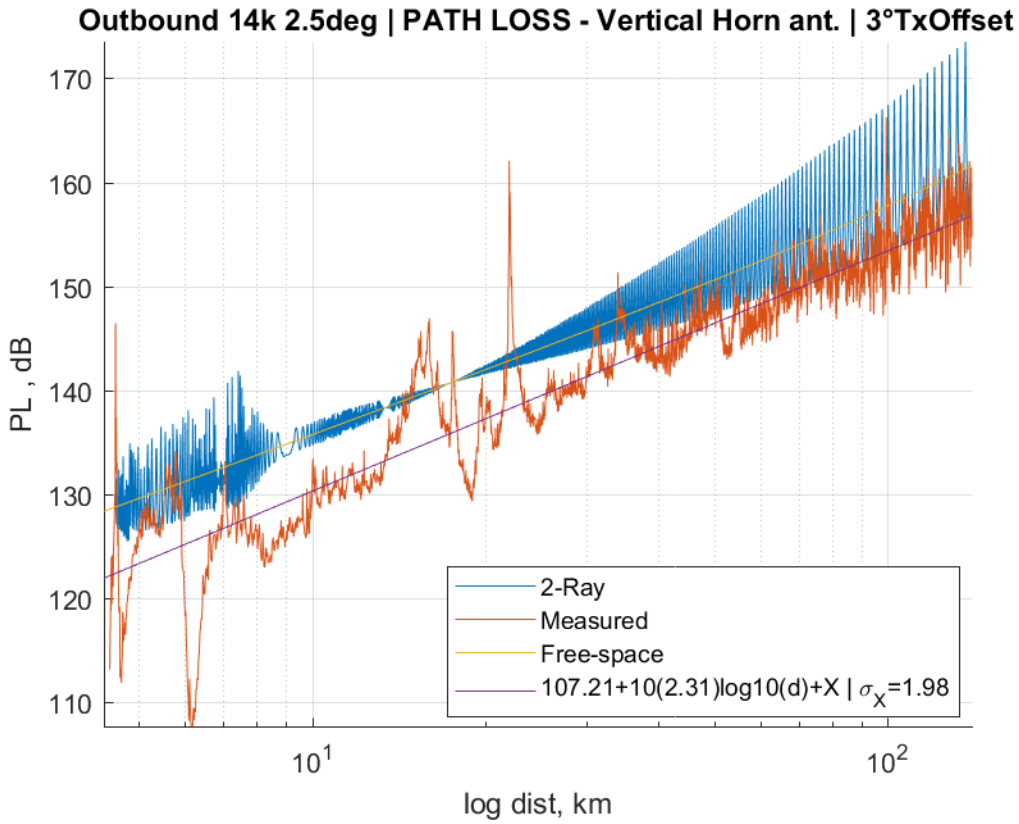

Figure A.24 Path loss for an outbound flight track with the vertical horn antenna.

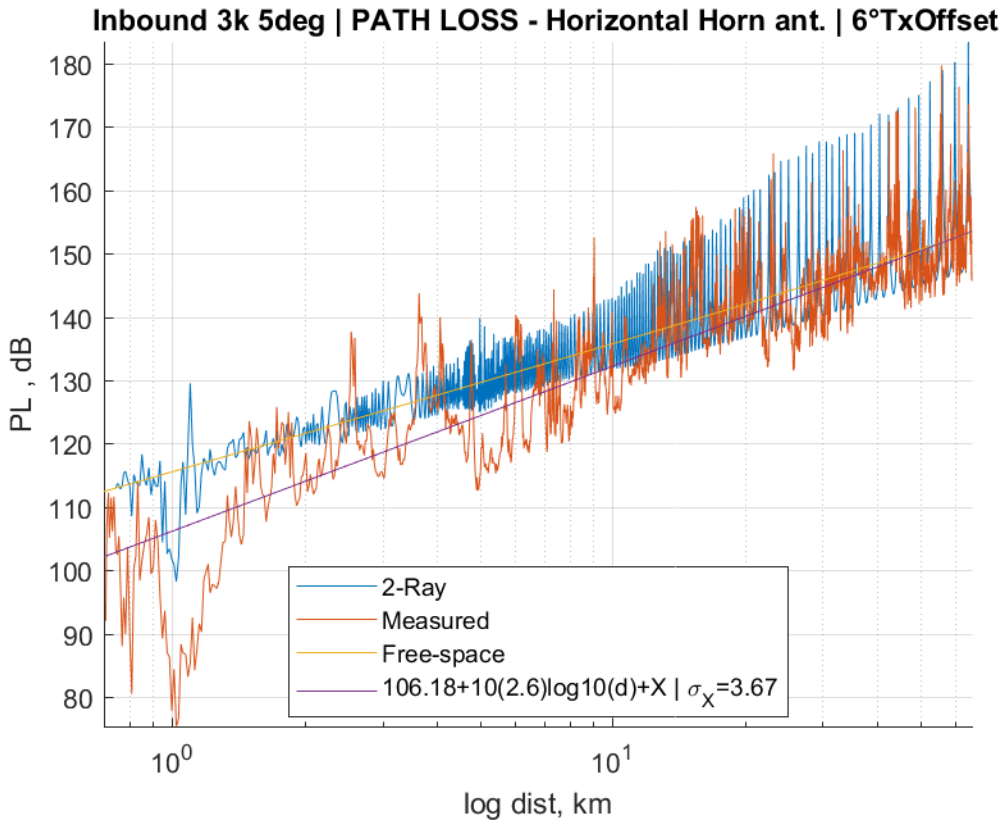

Figure A.25 Path loss for an inbound flight track with the horizontal horn antenna.

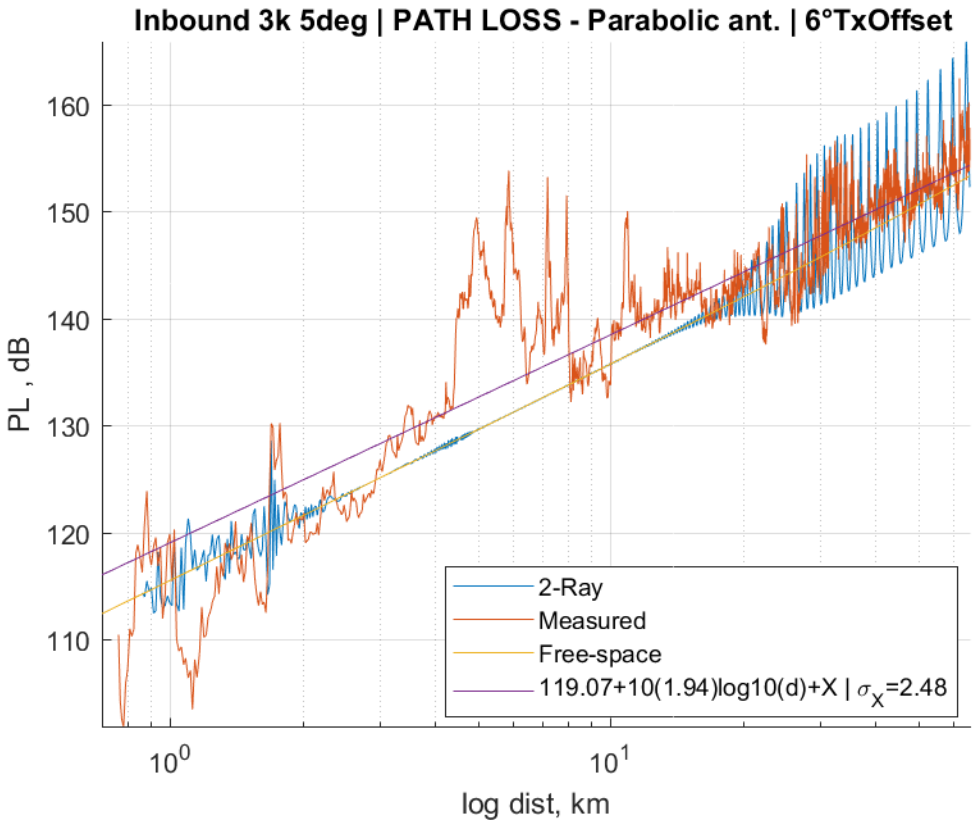

Figure A.26 Path loss for an inbound flight track with the parabolic antenna.

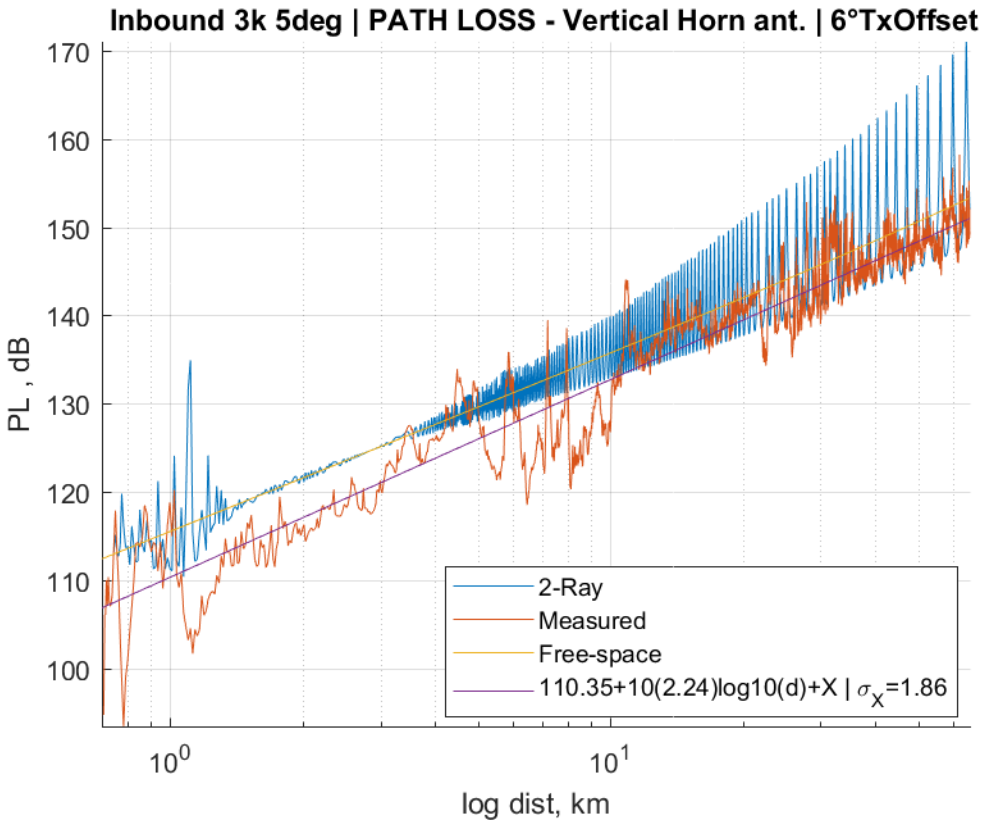

Figure A.27 Path loss for an inbound flight track with the vertical horn antenna.

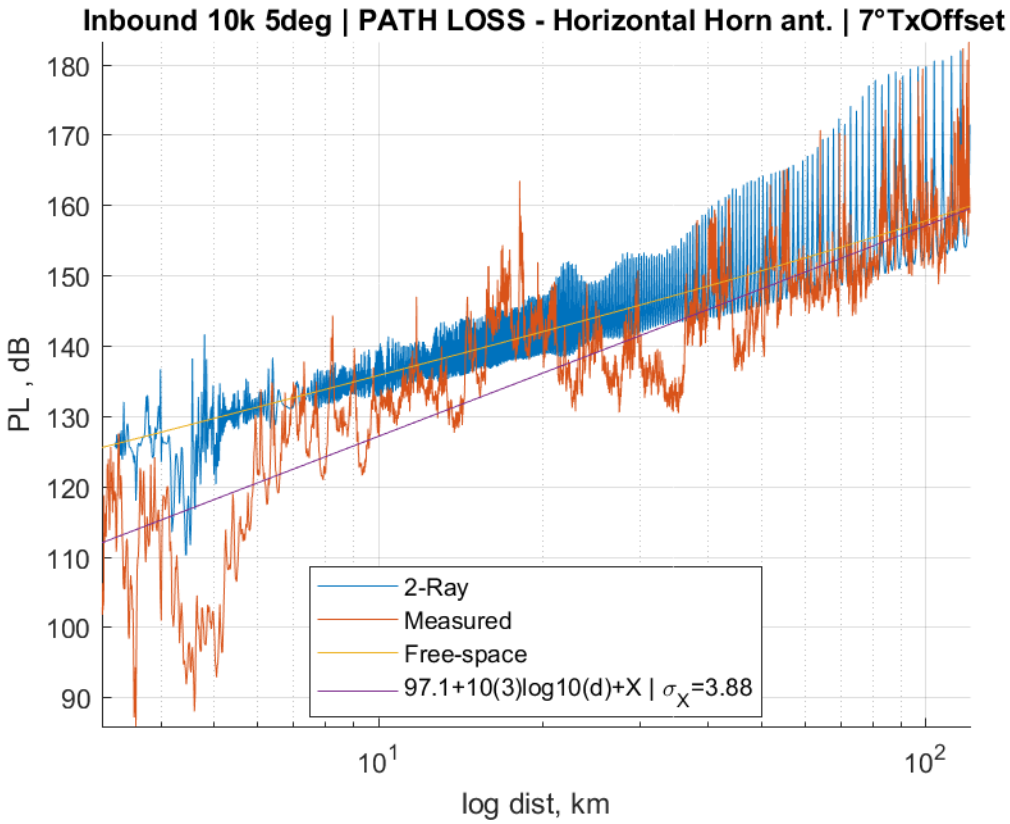

Figure A.28 Path loss for an outbound flight track with the horizontal horn antenna.

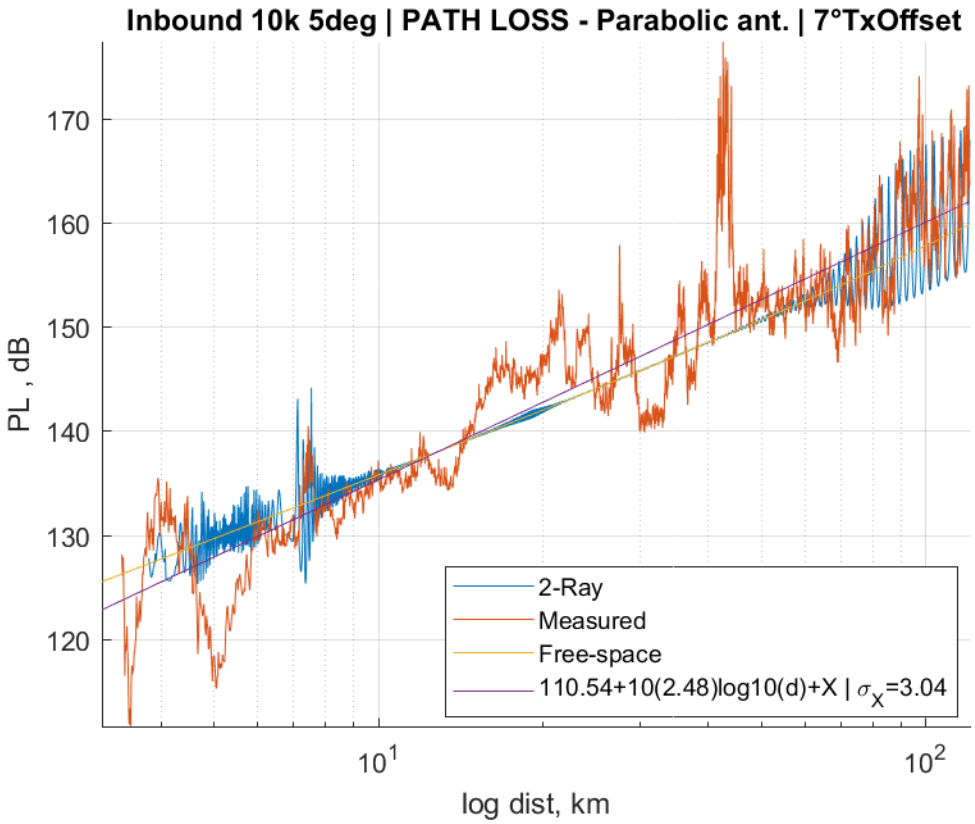

Figure A.29 Path loss for an inbound flight track with the parabolic antenna.

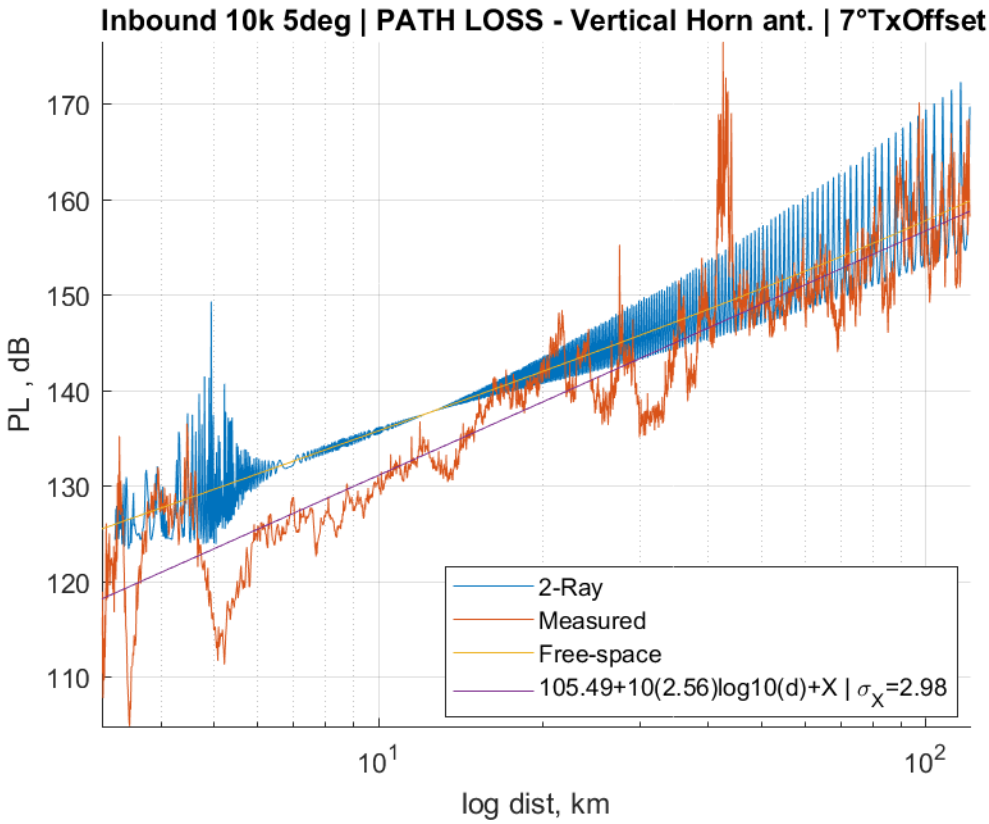

Figure A.30 Path loss for an inbound flight track with the vertical horn antenna.

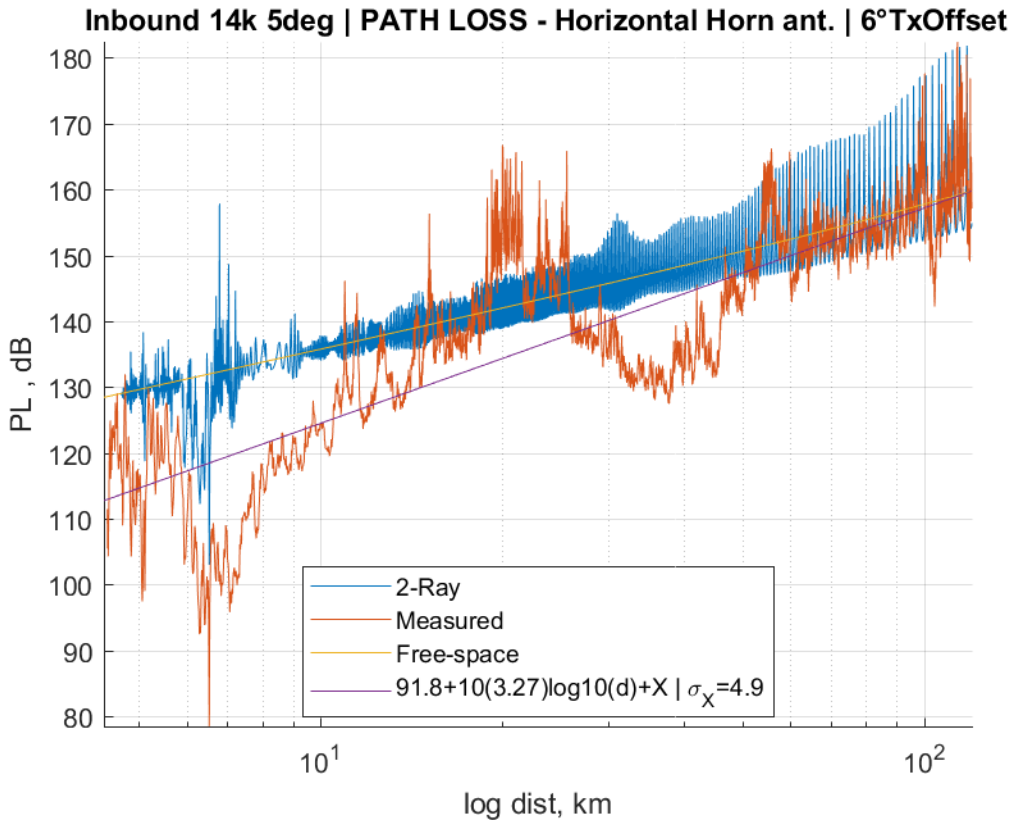

Figure A.31 Path loss for an inbound flight track with the horizontal horn antenna.

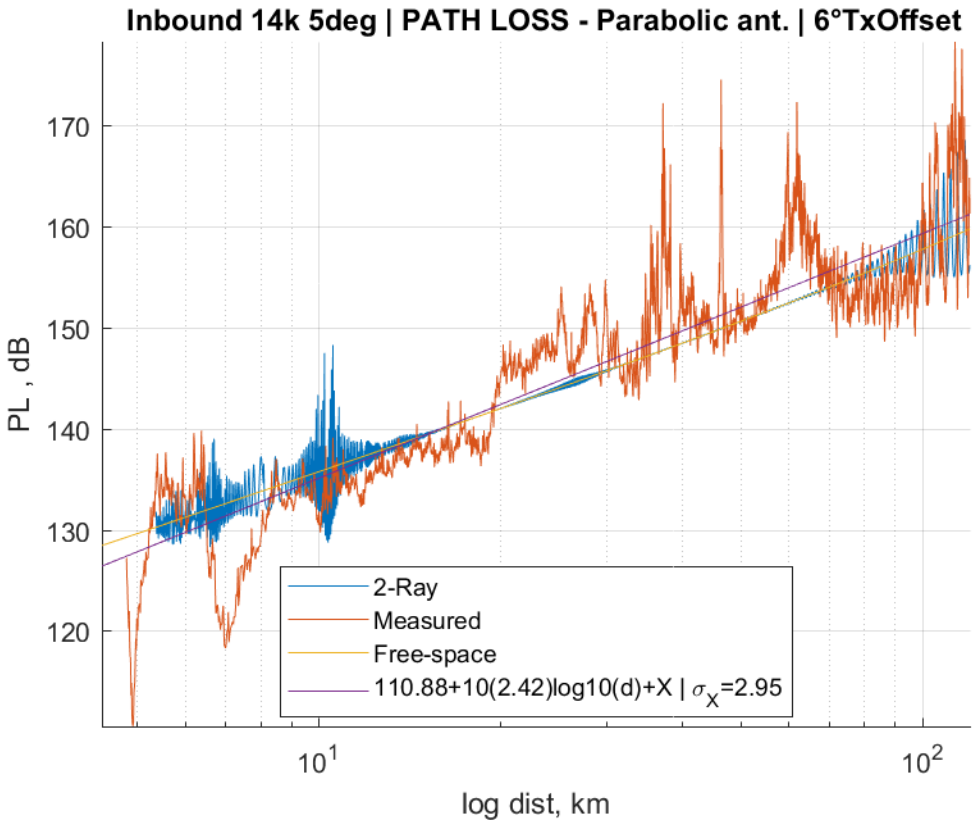

Figure A.32 Path loss for an inbound flight track with the parabolic antenna.

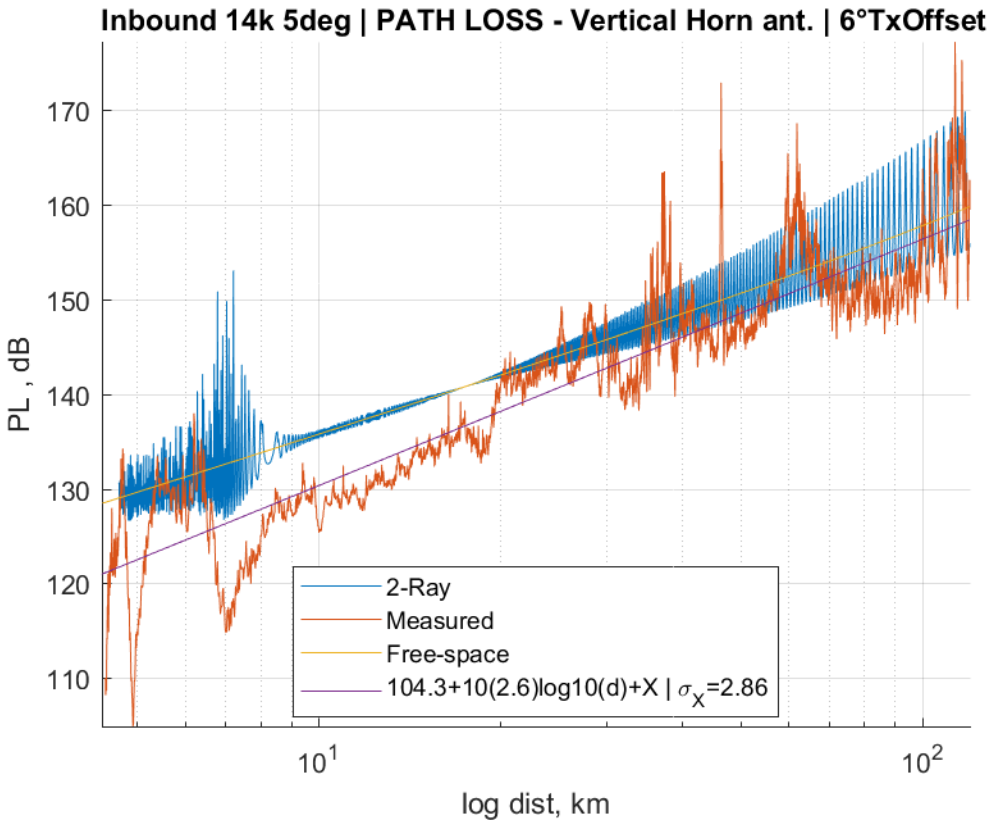

Figure A.33 Path loss for an inbound flight track with the vertical horn antenna.

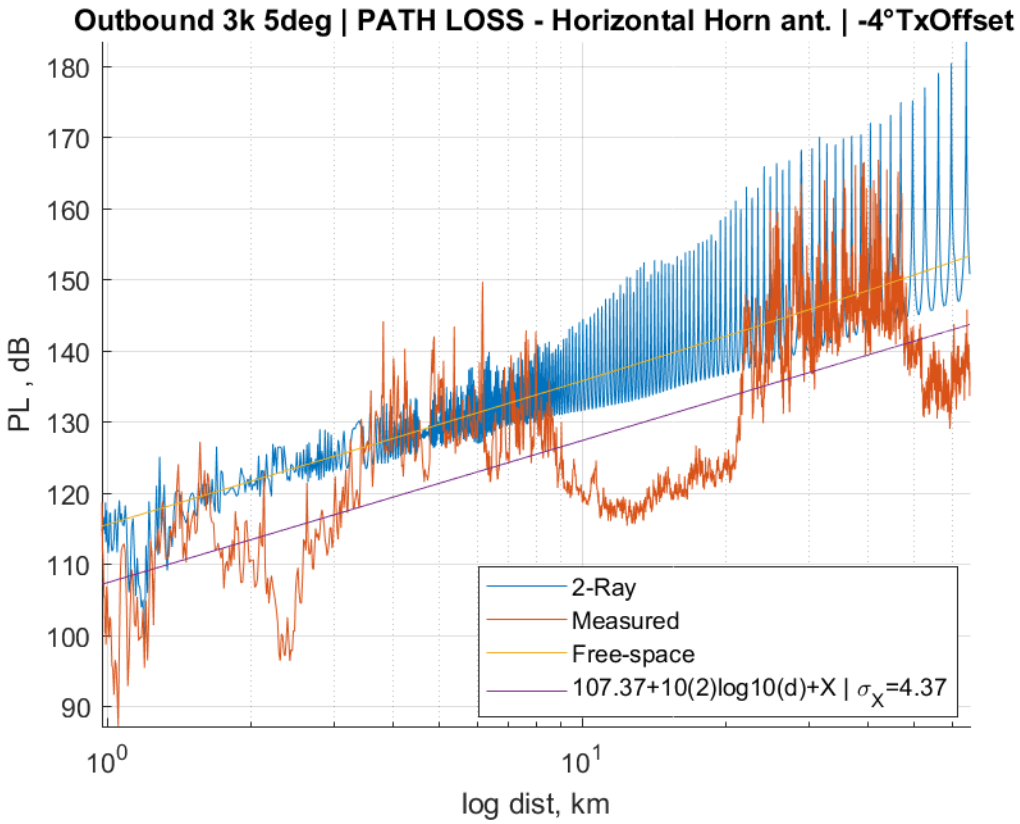

Figure A.34 Path loss for an outbound flight track with the horizontal horn antenna.

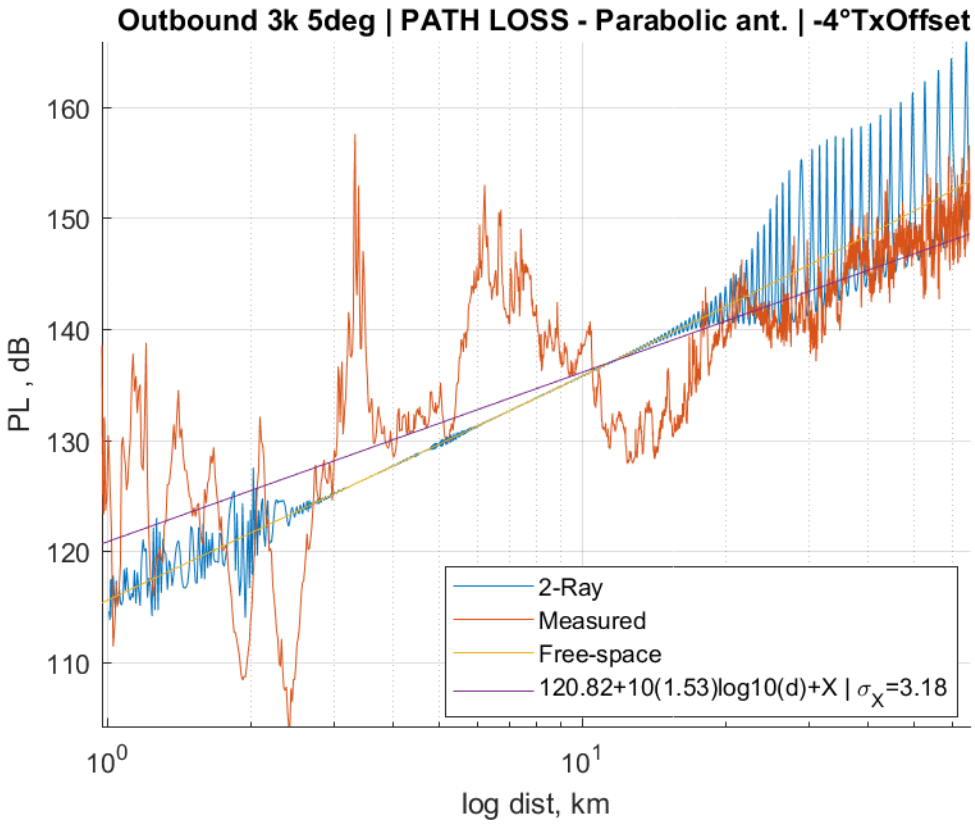

Figure A.35 Path loss for an outbound flight track with the parabolic antenna.

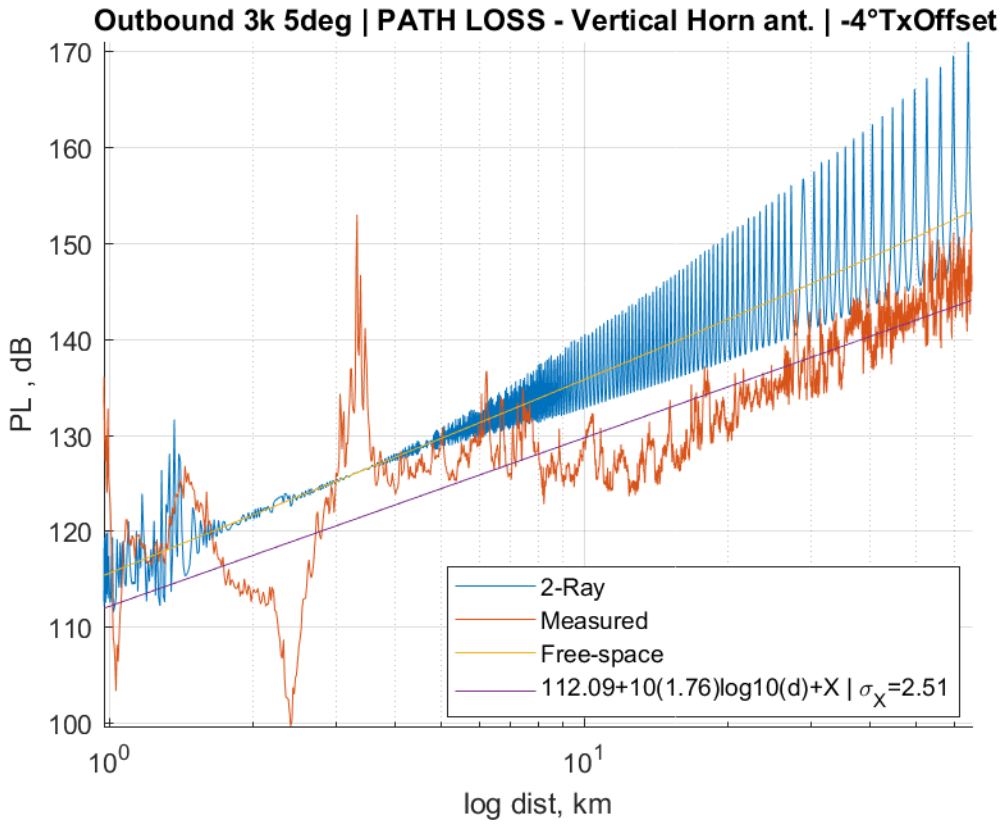

Figure A.36 Path loss for an outbound flight track with the vertical horn antenna.

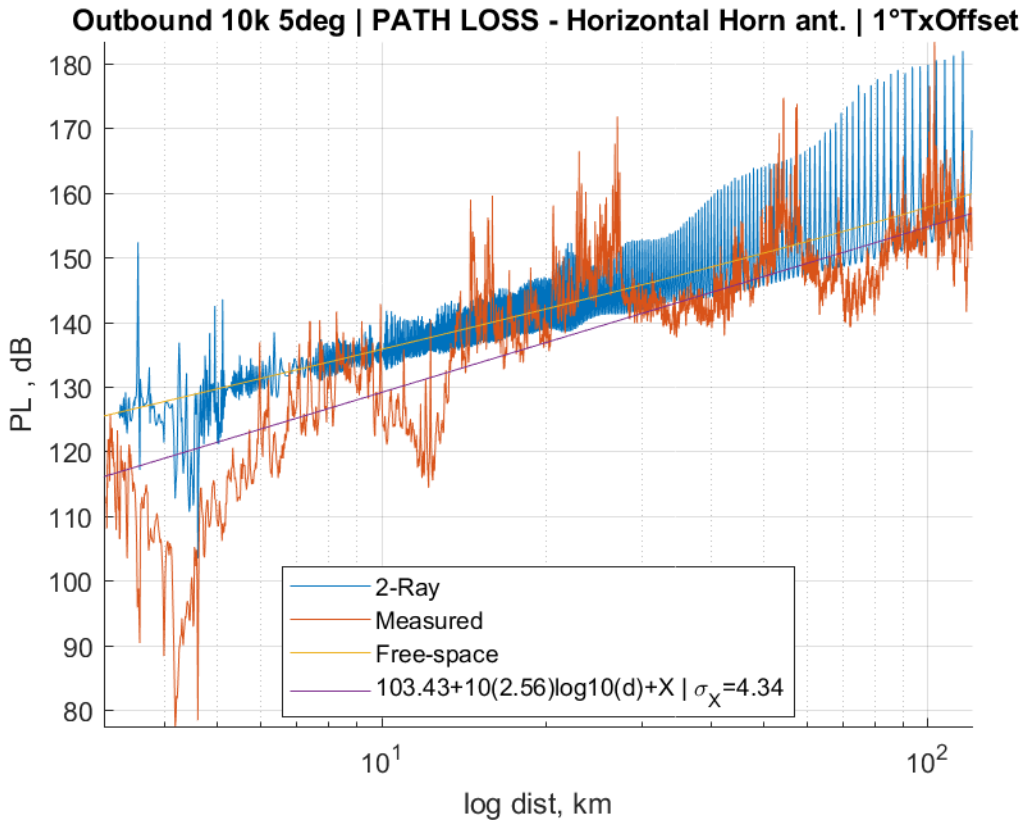

Figure A.37 Path loss for an outbound flight track with the horizontal horn antenna.

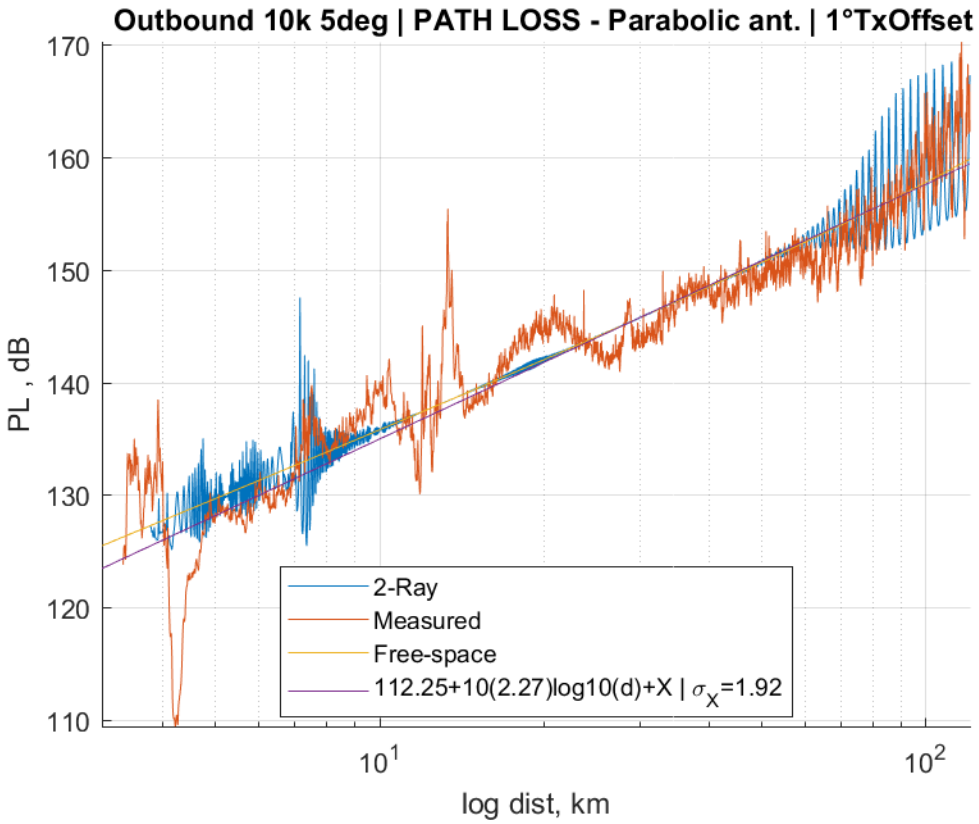

Figure A.38 Path loss for an outbound flight track with the parabolic antenna.

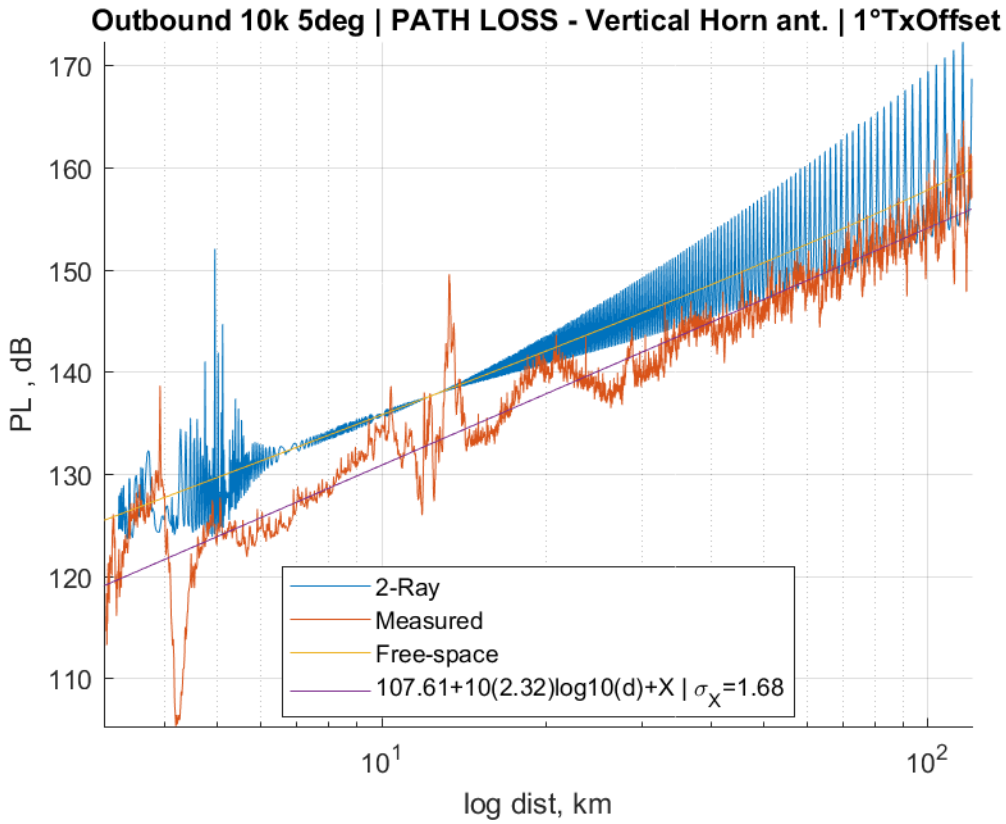

Figure A.39 Path loss for an outbound flight track with the vertical horn antenna.

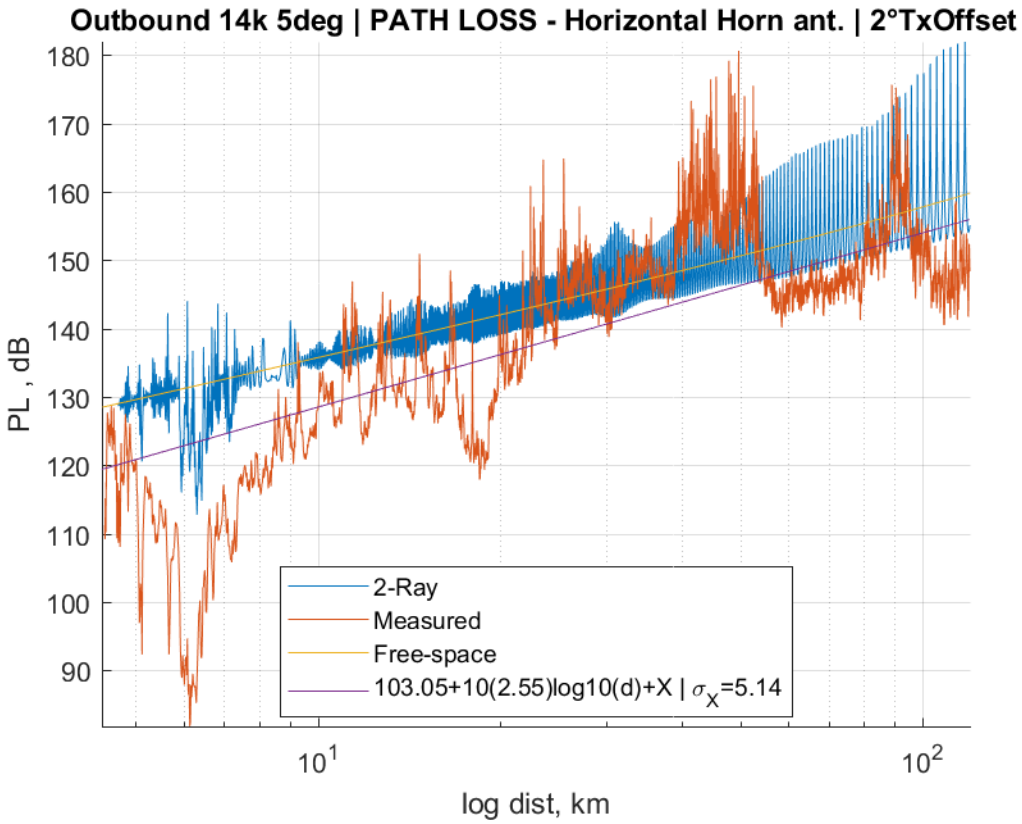

Figure A.40 Path loss for an outbound flight track with the horizontal horn antenna.

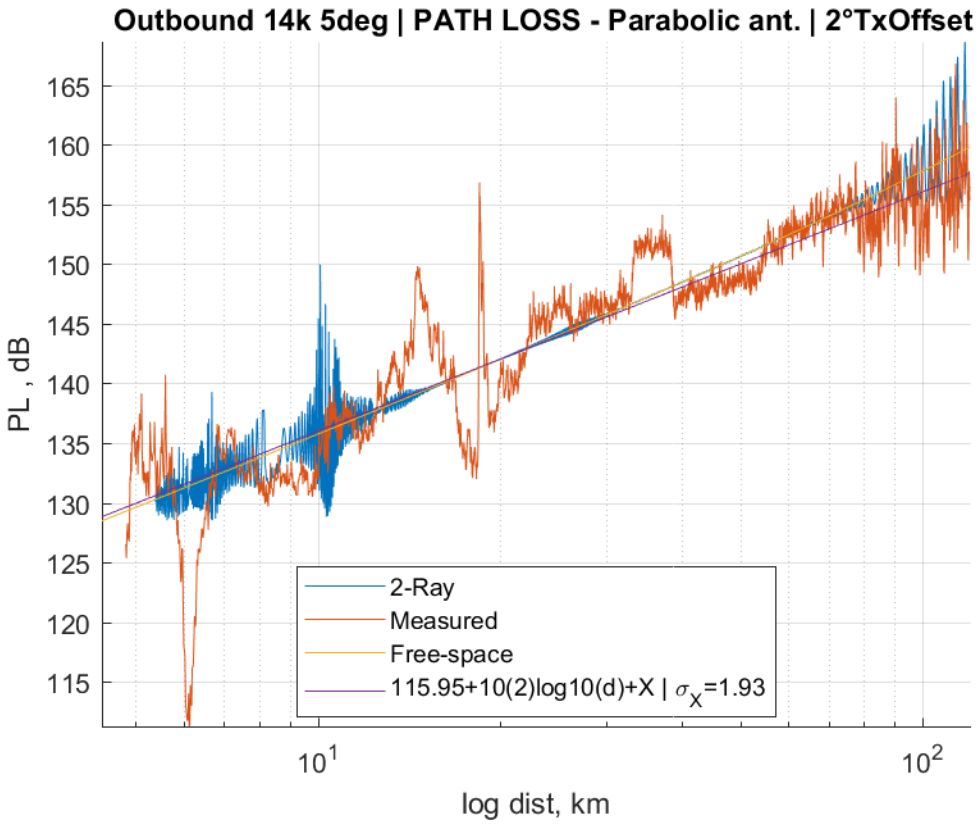

Figure A.41 Path loss for an outbound flight track with the parabolic antenna.

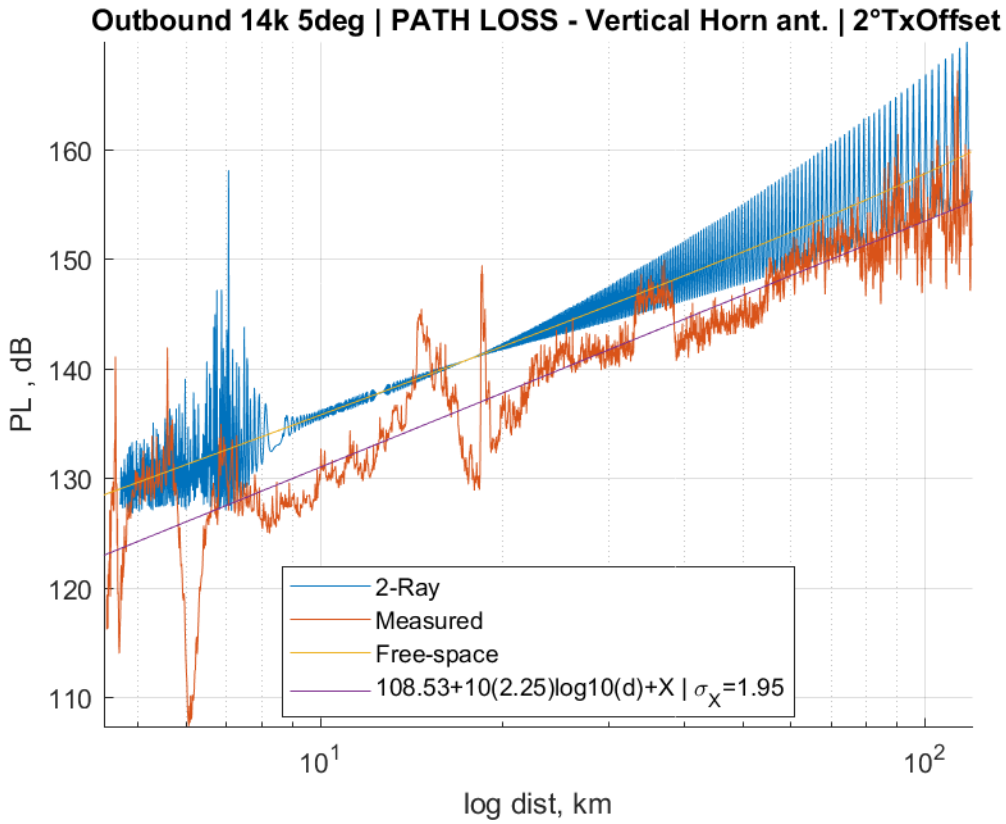

Figure A.42 Path loss for an outbound flight track with the vertical horn antenna.

APPENDIX B: Tables for log-distance path loss equation parameters

In this index, readers will find tables of log-distance fit equation parameters for the path loss curves for receiver inclination (elevation) angles 0 and 2.5 degrees and all corresponding flight tracks. These tables are similar to the table that appeared in Chapter 4, but they are separated into an appendix for readability.

Table B.1 Parameters for log-distance equations for a 0 degree RX inclination.

Flight Track (Offset, In/Out-bound, Altitude (ft), Inclination, Antenna)	**Path Loss Exponent**	**Offset**	**Std Dev (dB)**	ΔL_{max} **(dB)**
7°TXoffset Inbound 10k 0deg Parabolic	2.92	104.28	3.12	37.36
7°TXoffset Inbound 10k 0deg Vertical Horn	2.71	102.93	2.96	26.70
7°TXoffset Inbound 10k 0deg Horizontal Horn	3.37	92.87	4.32	29.70
7°TXoffset Inbound 14k 0deg Parabolic	2.97	101.10	3.60	38.93
7°TXoffset Inbound 14k 0deg Vertical Horn	2.60	102.94	3.31	35.79
7°TXoffset Inbound 14k 0deg Horizontal Horn	3.01	94.35	4.19	25.59
2°TXoffset Outbound 10k 0deg Parabolic	2.72	104.69	2.26	18.23
2°TXoffset Outbound 10k 0deg Vertical Horn	2.42	106.13	2.25	26.92
2°TXoffset Outbound 10k 0deg Horizontal Horn	2.26	104.13	3.62	17.59
0°TXoffset Outbound 14k 0deg Parabolic	2.77	105.03	2.42	25.12
0°TXoffset Outbound 14k 0deg Vertical Horn	2.23	108.12	1.98	9.81
0°TXoffset Outbound 14k 0deg Horizontal Horn	1.70	114.15	3.72	22.85

Table B.2 Parameters for log-distance equations for a 2.5 degree RX inclination.

Flight Track (Offset, In/Out-bound, Altitude (ft), Inclination, Antenna)	**Path Loss Exponent**	**Offset**	**Std Dev (dB)**	**ΔL_{max} (dB)**
5°TXoffset Inbound 10k 2.5deg Parabolic	3.08	102.12	2.33	18.81
5°TXoffset Inbound 10k 2.5deg Vertical Horn	2.63	103.42	2.47	13.39
5°TXoffset Inbound 10k 2.5deg Horizontal Horn	3.06	98.79	4.24	27.11
5°TXoffset Inbound 14k 2.5deg Parabolic	2.94	103.36	2.66	29.46
5°TXoffset Inbound 14k 2.5deg Vertical Horn	2.61	103.67	2.71	19.45
5°TXoffset Inbound 14k 2.5deg Horizontal Horn	3.17	95.03	4.35	27.84
0°TXoffset Outbound 10k 2.5deg Parabolic	2.44	108.92	2.31	18.24
0°TXoffset Outbound 10k 2.5deg Vertical Horn	2.03	110.51	1.97	15.68
0°TXoffset Outbound 10k 2.5deg Horizontal Horn	2.18	106.80	3.98	19.49
3°TXoffset Outbound 14k 2.5deg Parabolic	2.62	106.91	2.19	15.24
3°TXoffset Outbound 14k 2.5deg Vertical Horn	2.31	107.21	1.98	19.20
3°TXoffset Outbound 14k 2.5deg Horizontal Horn	2.80	100.35	3.74	25.78